ADVANCED FUNCTIONAL MATERIALS
www.afm-journal.de

# $H_2O_2$-Generating Advanced Nanomaterials for Cancer Treatment

*Kiyan Musaie, Samin Abbaszadeh, Kik Marais, Vahideh Nosrati-Siahmazgi, Saman Rezaei, Bo Xiao, Kamal Dua, Hélder A. Santos,* and Mohammad-Ali Shahbazi**

**Tumor cells exploit abnormal redox homeostasis and the pro-tumorigenic effect of reactive oxygen species (ROS) to enhance their survival and progression. However, excessively high levels of ROS can exceed the oxidative stress threshold of tumor cells, inducing cell death. This can occur by selectively elevating the concentration of $H_2O_2$ in tumor cells through both endogenous and exogenous mechanisms. The generated $H_2O_2$ serves as a precursor for toxic ROS, such as $^{\bullet}OH$ and $^1O_2$, via chemodynamic and photodynamic therapy, respectively, leading to apoptosis, necrosis, and ferroptosis. Strategies to boost $H_2O_2$ levels include direct delivery of exogenous $H_2O_2$ and amplifying endogenous $H_2O_2$ generation by inhibiting antioxidant enzymes, leveraging glucose oxidase, employing photocatalytic therapy (PCT), and utilizing metal peroxides. Among them, metal peroxides have displayed remarkable performance due to their excellent potential to elevate $H_2O_2$ concentration within tumor cells while simultaneously normalizing the acidic and hypoxic conditions of the tumor microenvironment (TME). Moreover, these nanostructures enhance tumor sensitivity to complementary treatments, like chemotherapy. This review summarizes advanced perspectives in the design, synthesis, and comparative analysis of $H_2O_2$-generating nanoplatforms, emphasizing their capacity to treat various cancers.**

## 1. Introduction

Cells constantly generate endogenous reactive oxygen species (ROS) as by-products of aerobic metabolism in the mitochondria and maintain redox homeostasis by regulating the balance between ROS formation and scavenging.[1] Excessive ROS, known as oxidative stress, damages lipids, proteins, and DNA, ultimately leading to cell death. Due to the higher metabolic irregularities and increased oncogenic signaling, tumor cells maintain elevated levels of intracellular $H_2O_2$, triggering the up-regulation of antioxidants, such as glutathione (GSH).[2]

Attempts have been made around the globe to develop more selective therapeutic strategies that exploit the inherent vulnerabilities of tumor cells to combat them. One such approach is manipulating reactive oxygen species (ROS) homeostasis in the tumor microenvironment (TME).[3] ROS, such as superoxide anion ($O_2^{\bullet-}$), hydrogen peroxide ($H_2O_2$), and hydroxyl radical ($^{\bullet}OH$) are a class of highly active

K. Musaie, K. Marais, H. A. Santos, M.-A. Shahbazi
Department of Biomaterials and Biomedical Technology
The Personalized Medicine Research Institute (PRECISION)
University Medical Center Groningen (UMCG)
University of Groningen
Antonius Deusinglaan 1, AV, Groningen 9713, Netherlands
E-mail: h.a.santos@umcg.nl; m.a.shahbazi@umcg.nl

S. Abbaszadeh
Department of Pharmacology and Toxicology
Faculty of Pharmacy
Urmia University of Medical Sciences
Urmia 57561-15327, Iran

The ORCID identification number(s) for the author(s) of this article can be found under https://doi.org/10.1002/adfm.202425866



**DOI: 10.1002/adfm.202425866**

V. Nosrati-Siahmazgi, S. Rezaei
Department of Pharmaceutical Biomaterials
School of Pharmacy
Zanjan University of Medical Sciences
Zanjan 45139-56184, Iran

B. Xiao
Department of Pharmacy
Personalized Drug Therapy Key Laboratory of Sichuan Province
Sichuan Academy of Medical Sciences & Sichuan Provincial People's Hospital
School of Medicine
University of Electronic Science and Technology of China
Chengdu 610054, China

K. Dua
Faculty of Health
Australian Research Centre in Complementary and Integrative Medicine
University of Technology Sydney
Ultimo, NSW 2007, Australia

K. Dua
Discipline of Pharmacy
Graduate School of Health
University of Technology Sydney
P.O. Box: 123 Broadway, Ultimo, NSW 2007, Australia

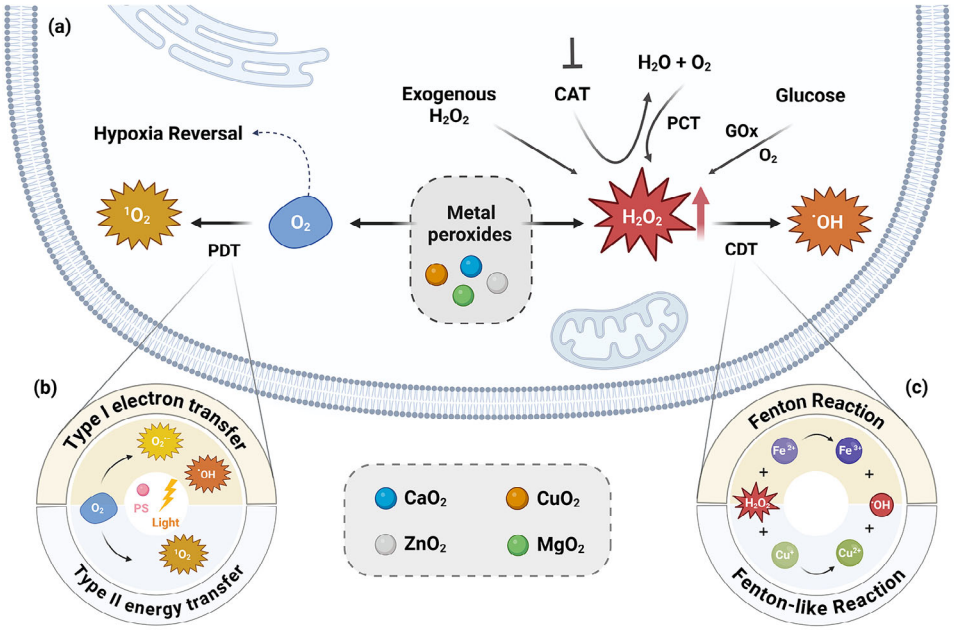


**Figure 1.** a) Schematic illustration of different strategies, in particular metal peroxides to increase the concentration of the $H_2O_2$ in TME. b) Influence of generated $O_2$ from metal peroxides in improving the outcome of the PDT. c) Influence of the generated $H_2O_2$ in improving the outcome of the CDT using Fenton/Fenton-like reactions. This figure is created on Biorender.com.

reduction products of oxygen.[1] One feasible approach in facilitating oxidative stress-mediated tumor cell death is to enhance the generation of $H_2O_2$, thereby, inducing chemodynamic therapy (CDT) and photodynamic therapy (PDT). In the presence of certain intracellular metal ions (e.g., iron), $H_2O_2$ contributes to Fenton or Fenton-like reactions, which convert it to highly toxic $^{\bullet}OH$, which is the basis of CDT.[4] Likewise, in the presence of photosensitizers and upon light irradiation, in situ generation of $O_2$ from intracellular $H_2O_2$ can lead to the production of the highly toxic $^1O_2$, which is the basis of the PDT.[5]

In recent years, several therapeutic strategies have been developed to exploit this vulnerability using $H_2O_2$ to mediate ROS formation.[4,6] While these strategies can overcome the side effects of standard cancer therapies, the intrinsic hypoxia of the TME significantly impairs their efficacy. Therefore, in addition to disrupting the oxidative balance of cancerous cells, the intracellular $H_2O_2$ can serve as a source for the catalytic generation of $O_2$ to attenuate the hypoxic TME and enhance hypoxia-limited treatment, such as photodynamic therapy (PDT), sonodynamic therapy (SDT), photothermal therapy (PTT) and starvation therapy (ST).

This review focuses on the role of $H_2O_2$ in the TME, ROS-based cancer therapy modalities, and various strategies to increase the concentration of $H_2O_2$ in the TME. The delivery of exogenous $H_2O_2$, the inhibition of antioxidative enzymes (glutathione peroxidase (GPx)), the in situ production of $H_2O_2$ by glucose oxidase, photocatalytic therapy (PCT), and metal peroxides are the strategies to increase the concentration of $H_2O_2$ that widely elaborated in this review (**Figure 1a**). Among various candidates, harnessing metal peroxides can induce oxidative stress-mediated cancer cell death via pH-dependent activity in a mildly acidic environment, resulting in GSH depletion and reversion of tumor hypoxia as indicators of TME remodeling. Understanding the potential of these approaches can pave the way for developing more effective and personalized cancer treatments.

## 2. Role of $H_2O_2$ in Cancer Cell Therapy

Among various ROS, $H_2O_2$ and $O_2^{\bullet-}$ are key redox signaling agents,[7] while $^{\bullet}OH$ and $^1O_2$ are the most reactive and toxic forms of oxidative stress.[8] Moreover, one of the unique physiological states of the TME that causes tumor progression is over-expressed $H_2O_2$.[9] This is due to the imbalance in the expression of enzymes related to the production of the $H_2O_2$-like manganese-dependent superoxide dismutase (SOD2/MnSOD) or removing $H_2O_2$-like catalase (CAT) and glutathione peroxidase 1 (GPx1).[10] SOD enhances the amount of $H_2O_2$ by converting superoxide anion ($O_2^{\bullet-}$) into $H_2O_2$ and catalase, and GPx1 decreases the amount of $H_2O_2$ by converting it to water and oxygen. This high concentration of $H_2O_2$ can act as a double-edged sword for cancer cells, allowing them to proliferate by activating transcription factors and inhibiting tumor suppressor genes at moderately elevated concentrations of $H_2O_2$; however, excessive levels can trigger apoptotic death.[11]

Furthermore, generated $H_2O_2$ can not only self-decompose into the $O_2$, promoting the outcome of $O_2$-related modalities like PDT and radiation therapy (RT), but it can also react with Fenton/Fenton-like reagents to produce highly toxic $^{\bullet}OH$ in CDT. This difference in the expression of the $H_2O_2$ in TME is a great opportunity to demonstrate innovative delivery properties by exploiting nanomaterials to create an imbalance in the oxidative equilibrium of cancer cells.

### 2.1. Photodynamic Therapy

PDT is an oxygen-dependent therapy that has become increasingly popular due to its negligible side effects, high selectivity, and reproducibility using photosensitizers, molecular oxygen, and light.[12] By absorbing light, photosensitizers transfer electrons to oxygen molecules, resulting in the production of $O_2^{\bullet-}$, $^1O_2$, and $^\bullet$OH, which can ultimately lead to cell death by apoptosis or necrosis (Figure 1b).[13] Despite substantial advancement in this area, the function of this modality is restricted by $O_2$ concentration, irradiation depth of the laser, and tolerance of photosensitizers in the TME. Accordingly, $H_2O_2$ generating nanoplatforms can overcome the limiting factor of the hypoxic TME by conversion of $H_2O_2$ to $O_2$.

### 2.2. Chemodynamic Therapy

CDT, which relies on Fenton/Fenton-like reactions to generate highly toxic $^\bullet$OH from $H_2O_2$,[14] has gained popularity owing to its specificity, low side effects, and no need for external stimuli (Figure 1c). Despite these advantages, the use of CDT in clinical settings is hampered by the inadequate amount of $H_2O_2$ in TME, the insufficiently low pH of the TME, and the high concentration of the antioxidant system (like GSH) in the TME. Thus, these criteria need further investigation to improve the outcomes and efficiency of CDT.

#### *2.2.1. Fenton/Fenton-Like Reaction*

In Fenton/Fenton-like reactions, mild acidic condition (pH 6.5) and increased concentration of the $H_2O_2$ in the TME triggers metal ions such as Fe,[15] Cu,[16] Mn,[17] Co,[18] and Au[19] to catalyze slightly toxic $H_2O_2$ to produce highly toxic $^\bullet$OH. These metal ions have been exploited in various nanostructures, including metal-organic frameworks (MOFs),[13] metal NPs,[20] quantum dots,[21] carbon dots,[22] nanodots,[23] liposomes,[24] dendrimers,[25] and nanosheets.[26] To improve the efficiency of nanoplatforms employing Fenton/Fenton-like reactions in unfavorable TME conditions, increasing the concentration of the $H_2O_2$ has been proposed to strengthen CDT efficiency in tumor cells.[27]

## 3. Strategies to Increase the Concentration of $H_2O_2$ in TME

Although cancer cells develop potent antioxidant systems, such as elevated levels of GSH and nicotinamide adenine dinucleotide phosphate (NADPH) to maintain redox homeostasis,[28] it is possible to disrupt this balance through external stimuli for cancer treatments, including chemotherapy, PDT, and CDT. For instance, chemotherapeutic agents like doxorubicin (DOX), paclitaxel, and cisplatin stimulate NADPH oxidase (NOX) activity to enhance $O_2^{\bullet-}$ generation, which is the precursor of $H_2O_2$, inducing cell apoptosis.[29] However, the intrinsic hypoxia of the TME significantly impairs the efficacy of these ROS-dependent therapies. $O_2$ not only is the power source of ROS production in chemotherapy and PDT, but also can regulate the transcription of hypoxia-inducible factor-1 (HIF-1), which is responsible for drug resistance and redox homeostasis maintenance in cancer cells. Moreover, the variable and often limited concentrations of $H_2O_2$ (10–50 µM) in different types of cancer cells restrict its transformation into adequate $^\bullet$OH and $O_2$ production.[30] Two feasible strategies have been proposed to supplement the cellular amount of $H_2O_2$: directly delivering exogenous $H_2O_2$ into cells or amplifying endogenous $H_2O_2$ generation. Approaches to amplify endogenous $H_2O_2$ generation are investigated through inhibiting antioxidant enzymes, utilizing glucose oxidase (GOx), applying photocatalytic therapy, and metal peroxides. Later, we will discuss the advantages and disadvantages of each approach in increasing $H_2O_2$ concentration.

### 3.1. Delivering Exogenous $H_2O_2$ in TME

Various strategies have been explored to deliver exogenous $H_2O_2$ into the TME (**Table 1**). These delivery platforms facilitate controlled release, increase tumor specificity, and reduce systemic toxicity. One of the primary approaches for delivering $H_2O_2$ is through nanocarriers, which can encapsulate the relatively unstable molecule and shield it from premature degradation in the bloodstream.[2b] One example involves $H_2O_2$-$H_2O$-filled poly(methyl methacrylate) microcapsules to allow for the controlled release of $H_2O_2$ and oxygen at the tumor site.[31] Likewise, $H_2O_2$-loaded liposomes ($H_2O_2$@liposome) alongside CAT-loaded liposomes (CAT@liposome) allow for the dual delivery of oxygen and $H_2O_2$.[32] This exogenous $H_2O_2$ acts as fuel for CAT, resulting in the reversal of hypoxic and immunosuppressive TME.

However, these approaches still face challenges due to the potential premature $H_2O_2$ release in the bloodstream, which can lead to systemic oxidative damage and diminished therapeutic efficacy.

### 3.2. Preventing $H_2O_2$ Consumption in TME by Inhibiting Antioxidant Enzymes

One significant barrier to the effectiveness of $H_2O_2$-based cancer therapies is the tumors' inherent ability to neutralize $H_2O_2$, through elevated antioxidant defenses. To overcome these ROS-scavenging defenses, several approaches have been developed to maximize the impact of therapies, such as inhibiting the enzymes responsible for $H_2O_2$ breakdown, particularly catalase (CAT) and glutathione peroxidase 4 (Gpx4) (Table 1). These enzymes play crucial roles in neutralizing ROS, thereby protecting cancer cells from oxidative damage.

CAT is an antioxidant enzyme abundantly expressed in many tumors, catalyzing the conversion of $H_2O_2$ into water and oxygen, significantly reducing the cytotoxic effects of $H_2O_2$.[33] Targeting CAT with specific inhibitors has become a pivotal approach in cancer therapy, as inhibiting its activity enables higher concentrations of $H_2O_2$ to accumulate within tumors. Especially CAT inhibitors, in combination with ROS-generating systems, can lead to enhanced oxidative stress and a significant increase in cancer cell apoptosis. For instance, 3-amino-1,2,4-triazole (3-AT) has

 

**Table 1.** Critical paradigms of different biomaterials utilizing various mechanisms for increasing the concentration of $H_2O_2$ for cancer therapy.

| Mechanism of action | Nanomaterial | Size | Dose in vitro (cell viability); in vivo | Type of cancer | In vitro cell line | In vivo model | Application | Refs. |
|---|---|---|---|---|---|---|---|---|
| Exogenous $H_2O_2$ | $H_2O_2$/$Fe_3O_4$–PLGA polymersome | 412 nm | – 5 mg $kg^{-1}$ | Cervical carcinoma | HeLa | HeLa bearing BALB/cAnN | CDT/magnetic resonance imaging | [42] |
| Exogenous $H_2O_2$ | PMMA microcapsules | 5–30 µm | – | – | – | – | – | [31] |
| Exogenous $H_2O_2$ | CAT@liposome; $H_2O_2$@liposome | 140 nm | 40 µg $mL^{-1}$ of CAT and 50 mM of $H_2O_2$; 0.3 mg of CAT and 0.1 mmol per mouse | Breast | 4T1 | 4T1; CT26; prostate PDX bearing BALB/c | Radio-immunotherapy | [32] |
| GOx-mimicking activity | UMOFs@Au NPs | 30 nm | 10 µg $mL^{-1}$ (13%); — | Glioblastoma | U87MG | U87MG bearing athymic nude mice | PDT | [38] |
| GOx-mimicking activity | P@Pt@P-Au-FA nanoreactor | 148 nm | 100 µg $mL^{-1}$ (10%); 200 µg per mouse | Breast | 4T1 | 4T1 bearing BALB/c | PDT/ST | [36] |
| GOx-mimicking activity | GMOF-LA nanosheets | N/A | 80 µg $mL^{-1}$ (18.6%); 5 mg $kg^{-1}$ | Glioblastoma | U87MG | U87MG-bearing nude mice | PDT/NO-mediated gas therapy | [37] |
| Inhibiting anti-oxidant enzymes | CAT-Ce6/F-PEI NPs | 343 nm | 0.8 µg $mL^{-1}$ of Ce6 (≈20%); 3 mg $kg^{-1}$ of Ce6 | Bladder | T24 | T24 bearing BALB/c nude mice | PDT | [34] |
| Inhibiting anti-oxidant enzymes | Self-assembled Cis-CD-Fc supramolecular NPs | 92 nm | 700 nM of Cis (≈50%); 2 mg $kg^{-1}$ of Cis | Breast | 4T1 | 4T1 bearing BALB/c | CDT/chemotherapy | [43] |
| Photocatalysis | GQD/P-$C_3N_4$ composite | 90 nm | 200 µg $mL^{-1}$ (10%); 8 mg $kg^{-1}$ | Breast | 4T1 | 4T1 bearing BALB/c | PCT | [39] |
| Photocatalysis | ICG-loaded aptamer-functionalized COF-Pt nanozyme | N/A | 200 µg $mL^{-1}$ (≈20%); 8 mg $kg^{-1}$ | Breast | 4T1 | 4T1 bearing BALB/c | PCT/PTT | [44] |

Abbreviations: CAT: catalase; CD-Fc: $\beta$-cyclodextrin-ferrocene conjugates; Ce6: Chorin-e6; Cis: cisplatin (IV); COF: covalent organic frameworks; FA: folic acid; F-PEI: fluorinated polyethylenimine; GMOF: Au NPs modified Zr-TCPP MOF nanosheets; GQD: graphene quantum dots; ICG: indocyanine green; LA: L-Arg; P: porphyrin metal-organic frameworks; P-$C_3N_4$: phosphorus-doped carbon nitride; PDX: patient-derived xenograft; PLGA: poly lactic-co-glycolic acid; PMMA: polymethyl methacrylate; Pt: platinum nanoparticles; UMOFs: unconventional metal-organic frameworks.

been explored as a catalase inhibitor that enhances ROS accumulation in cancer cells, improving PDT and CDT efficacy by limiting the breakdown of $H_2O_2$.[34]

### 3.3. $H_2O_2$ Production from Glucose

Cancer cells exhibit an increased reliance on glucose, suggesting that inducing a glucose deprivation process could improve anticancer therapeutic efficiency.[35] GOx catalyzes the oxidation of gluconic acid and $H_2O_2$, depleting the TME of glucose and inducing starvation therapy. Numerous researchers have designed GOx-mimicking systems that make use of glucose deprivation while simultaneously converting the $H_2O_2$ to cytotoxic $^1O_2$[36] or NO,[37] thus realizing synergistic cancer therapy with improved efficacy (Table 1).

For example, Mu et al. designed a planar MOF-based composite (GMOF-LA) by incorporating ultrasmall Au NPs and L-Arginine for combined PDT and NO-mediated gas therapy to ablate cancer cells (**Figure 2a**).[37] The zirconium-porphyrin-based MOF nanosheets Zr-TCPP (tetrakis(4-carboxyphenyl)porphyrin) were initially synthesized through a solvothermal reaction, where TCPP and Zr6 clusters act as heme-like ligands and metal nodes, respectively (Figure 2b). The ultrasmall Au NPs were incorporated via an in situ reduction method on the surface of MOF nanosheets (Figure 2c,d). PEGylation by (PEG)n-COOH allowed for better biological circulation. The GMOFs showed sufficient GOx-mimicking activity, whereby the Au NPs catalyze the conversion of glucose into $H_2O_2$ and gluconic acid in the presence of $O_2$ (Figure 2e). A high level of NO was observed at the LA: GMOF ratio of 2:1, indicating that the generated $H_2O_2$ could initiate the oxidation of l-Arg into NO. Both MOF and GMOF nanosheets exhibited negligible toxicity to U87MG; however, ROS-based PDT, NO-mediated gas therapy, and the combination treatment group (GMOF-LA + laser) significantly decreased the cell viability, with the combination treatment group being the most effective (Figure 2g). This was linked to therapeutic efficacy, as a combination-treated group showed significantly inhibited tumor growth compared to the PDT-based treatment and gas therapy group.

In another work, MOF-based core–shell UMOF@Au NPs were designed to decompose glucose into $H_2O_2$, followed by generating $O_2$ from $H_2O_2$ under NIR laser irradiation.[38] To synthesize these UMOF@Au NPs, Yb-rich core–shell upconversion NPs (UCNPs) were first synthesized using a solvent thermal method. Thereafter, oleic acid stabilized UCNP was

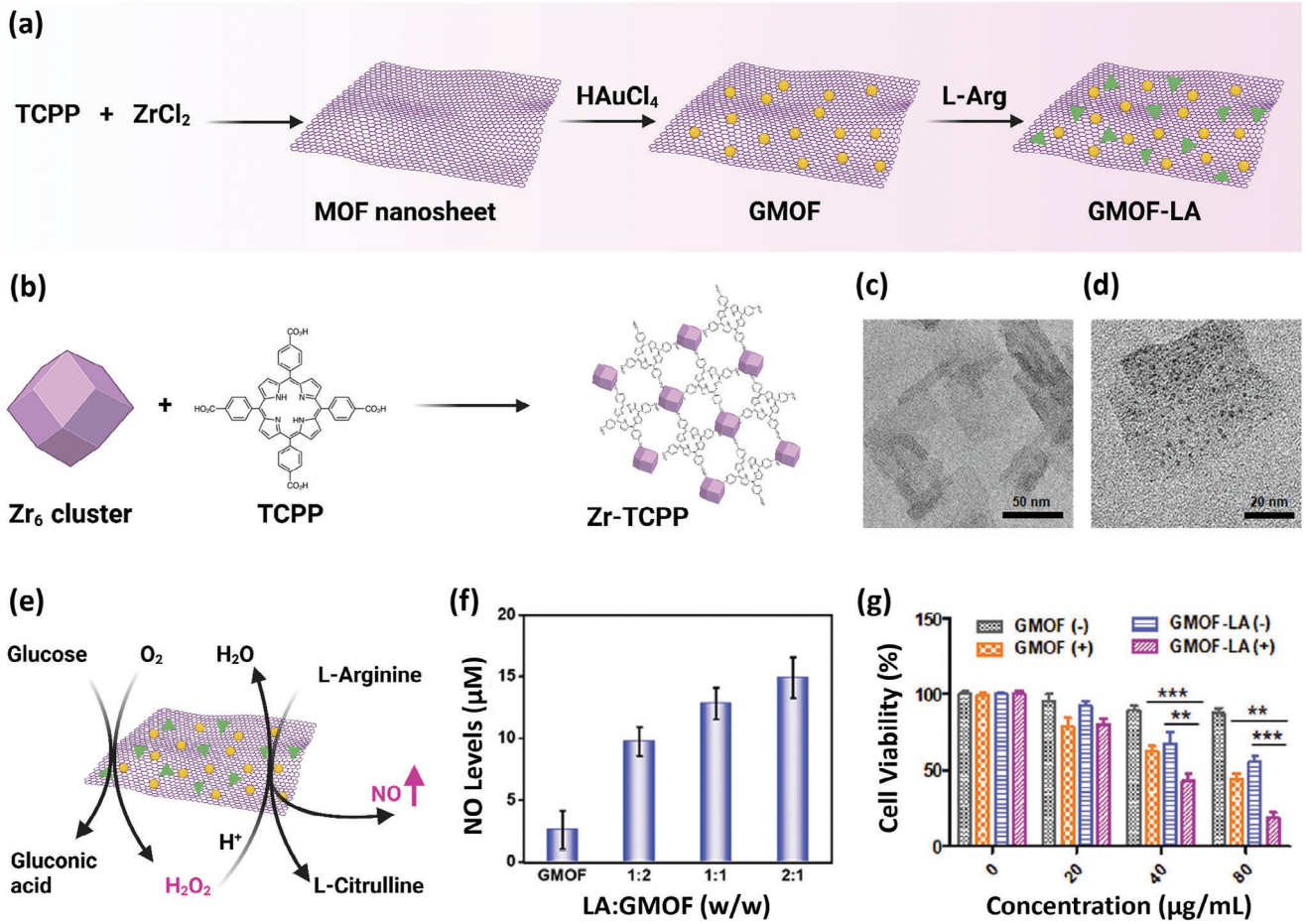


**Figure 2.** a) The schematic illustration of synthesizing GMOF-LA nanosheets. Created on Biorender.com. b) Formation of the 3D nanoporous framework of the Zr-TCPP MOF nanosheets via the linkage of tetra-topic ligand TCPP and $Zr_6$ cluster. Created on Biorender.com. c,d) TEM images of the synthesized 2D MOF nanosheets and Au NPs loaded nanosheets (GMOF), respectively. e) Schematic illustration representing the cascade reaction facilitated by ultrasmall Au NPs loaded onto MOF nanosheets. The ultrasmall Au NPs catalyze the glucose to produce $H_2O_2$, resulting in the potential subsequent oxidization of l-Arg into NO. Created on Biorender.com. f) Evaluation of NO production by the Griess assay. g) In vitro studies: cytotoxicity of U87MG cells under different treatments after 24 h of incubation. $^{**}p < 0.01$, $^{***}p < 0.001$. Reproduced with permission.[37] Copyright 2020, Wiley.

ligand-exchanged with 3,4-dihydroxyhydrocinnamic acid to obtain carboxy acid functionalized products. Finally, Au NPs were integrated into the UMOFs matrix by reducing $HAuCl_4$ with $NaBH_4$. Upon NIR excitation, the UCNPs could harvest low-energy photons and emit light, which could be absorbed by the outer MOF shells via fluorescence resonance energy transfer (FRET), thereby producing cytotoxic $^1O_2$ for PDT applications. In vitro, UMOFs@Au NPs showed intracellular $H_2O_2$ production, although not as efficiently as AuNPs alone. Additionally, under hypoxic conditions, UMOF@Au NPs showed promising $O_2$-depleting ability. The greatest cytotoxic ability against U87MG cells was noted when treated with UMOF@Au NPs under laser irradiation. The treatment efficacy of UMOF@Au NPs was confirmed in vivo in U87MG tumor-bearing mice, as tumors treated with UMOF@Au NPs under laser irradiation demonstrated 100% tumor eradication eight days post-injection with no observed tumor recurrence. In another study, Liu et al. designed an in situ catalytic cascade model for a synergistic therapeutic strategy driven by dual-nanozymes-engineered porphyrin MOF (PCN).[36] First, the uniformed PCNs with an average diameter of 54 nm were produced, and PVP-coated cisplatin NPs (3.5 nm) were attached to the surface via electrostatic and coordination interactions and further sandwiched by a shell of PCN (P@Pt@P) (**Figure 3a**). Further stabilizing of Au NPs on the P@Pt@P shell was employed (P@Pt@P−Au) and folic acid (FA) was introduced (P@Pt@P−Au−FA). P@Pt@P showed significant production of $^1O_2$ after the addition of $H_2O_2$ under hypoxic conditions (Figure 3b), indicating hypoxia relief via the conversion of $H_2O_2$ to $O_2$, which could be utilized for $^1O_2$-induced PDT. The GOx-mimicking ability of the Au NPs in P@Pt@P−Au was also confirmed by the wide absorbance of gluconic acid (Figure 3c). The in vivo accumulation of P@Pt@P−Au−FA was tracked by its near-infrared fluorescence emission ability and reached its maximum in the 4T1 tumor region of the mice 22 h after intravenous injection (Figure 3d). Additionally, subsequent tumor oxygenation was observed almost at a maximum of 8 h after injection (Figure 3e). The P@Pt@P−Au−FA-treated group under laser exposure exhibited a high inhibition ratio of 4T1 tumor cells (90.9%) in vivo (Figure 3f), and no metastatic sites were observed in the lungs of mice treated with P@Pt@P–FA– or

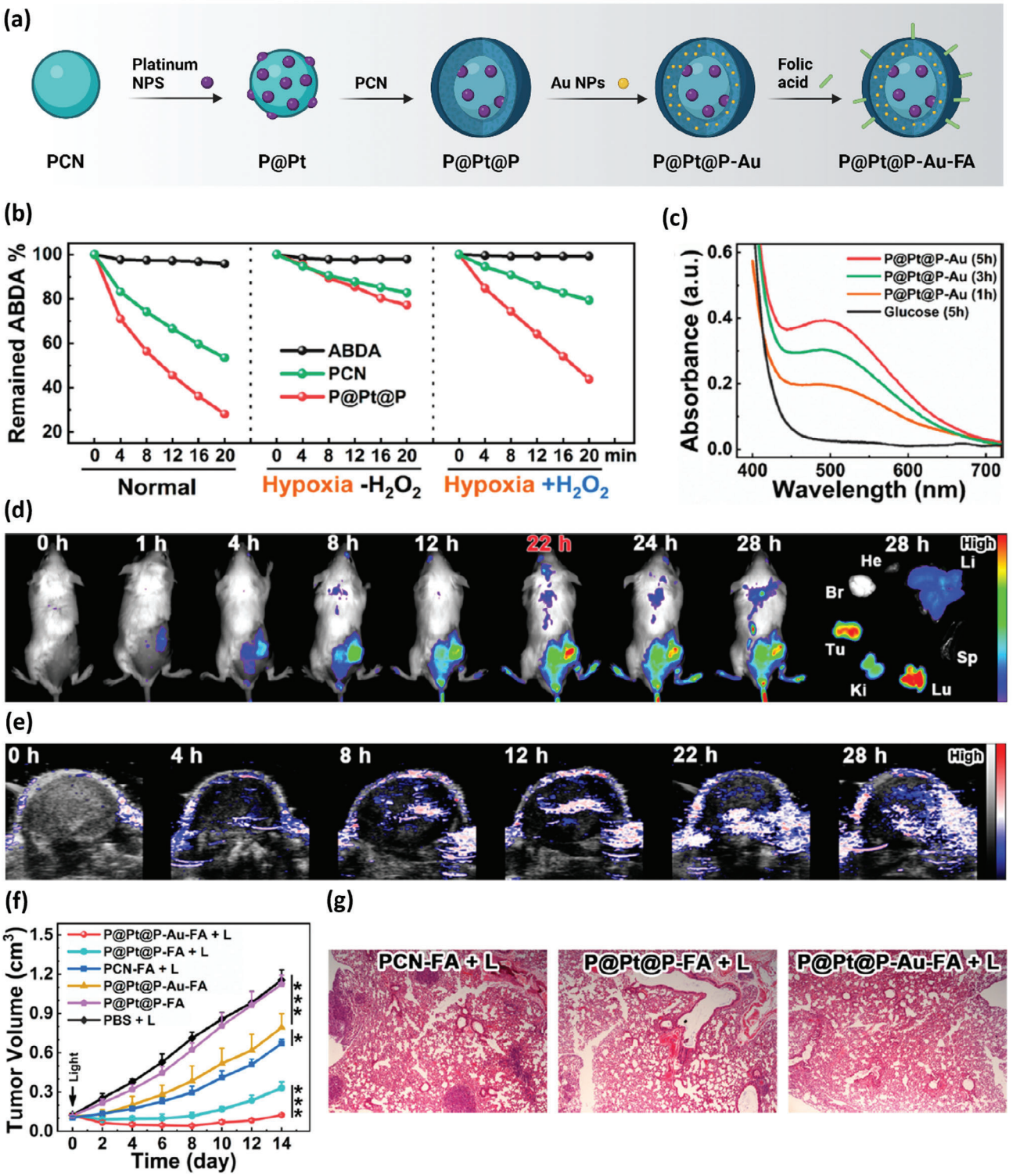


**Figure 3.** a) Schematic illustration of the catalyst-driven cascades-enhanced synergistic cancer therapy utilizing dual inorganic nanozymes-engineered PCNs. Created on Biorender.com. b) PDT efficacy of PCN (100 μg $mL^{-1}$) or P@Pt@P (100 μg $mL^{-1}$) under three different conditions upon 671 nm laser exposure (300 mW $cm^{-2}$), evaluated by calculating the remaining percentage of ABDA (a $^1O_2$ sensor). c) Glucose oxidase-mimicking capability of P@Pt@P–Au. d) In vivo fluorescence imaging of 4T1 tumor-bearing mice injected with P@Pt@P–Au–FA at different time intervals. e) Oxygen saturation level of 4T1 tumor-bearing mice injected with P@Pt@P–Au–FA at different time intervals. f) Tumor growth curves of the 4T1 tumor-bearing mice treated with different groups (300 mW $cm^{-2}$ for 8 min of 671 nm laser irradiation, $n = 6$). $p$-values: Student's $t$ test, ***$p < 0.001$, **$p < 0.01$, and *$p < 0.05$. g) H&E staining of representative lungs of the mice in the control group and the PDT-treated groups on day 14. Reproduced with permission.[36] Copyright 2019, Wiley.

P@Pt@P−Au−FA− after laser exposure (Figure 3g). These results confirm the catalase-mimicking cisplatin (Pt) NPs with excellent intra-tumoral $O_2$-evolving ability, thereby 1) improving the $O_2$-dependent PDT and 2) providing the supply of $O_2$ for depletion of glucose by Au NPs for synergistic starving-like therapy with self-produced $H_2O_2$ as a substrate for Pt NPs. Therefore, the unique potential of MOFs-supported nanozymes is a promising candidate for combating solid tumors by providing bioinspired nanoreactor-mediated therapy.

### 3.4. $H_2O_2$ Production from $H_2O$ and $O_2$

Photocatalytic therapy (PCT) has emerged as a method for in situ $H_2O_2$ generation at tumor sites under very mild conditions using $O_2$ and $H_2O$ in the presence of visible light.[39] Various photocatalysts, including carbon nitride ($C_3N_4$ or $C_5N_2$) and titanium dioxide ($TiO_2$), have been reported as promising candidates for $H_2O_2$ generation.[40] For instance, the production of $H_2O_2$ from the $CaO_2$.cisplatin@$Fe_3O_4$.$C_3N_4$ nanocomposite was evaluated for colon cancer therapy through synergistic CDT/PCT/chemotherapy.[41] In order to observe efficient CDT performance, high concentrations of $H_2O_2$ are demanded. In this platform, the $H_2O_2$ generated from a metal peroxide ($CaO_2$) was doubled by the photocatalytic activity of $C_3N_4$. In fact, photocatalysis enabled the production of $H_2O_2$ molecules from the adsorbed $H_2O$ on g-$C_3N_4$ through a two-electron transfer route under irradiation. The elevated $H_2O_2$ concentration resulted in the inhibition of colon cancer growth in both in vitro and in vivo experiments. In another study, phosphorus-doped $C_3N_4$ supported graphene quantum dots (GQD/P-$C_3N_4$) were developed for photo-induced catalytic cancer therapy.[39] To enhance light penetration depth, an NIR laser was used instead of visible light. GQD, by converting NIR to visible light, excites P-$C_3N_4$ to generate $H_2O_2$. Finally, the abundant $H_2O_2$ was converted to $^{\bullet}OH$ by GQD to kill cancer cells. Furthermore, this platform exhibited satisfactory anti-tumor efficiency while showing desirable biosafety in vivo. This proof-of-concept design offers an interesting approach to inhibit tumor growth by accelerated ROS and solving the low penetration depth of the visible light for photocatalytic systems. At present, the efficient generation of $H_2O_2$ from photocatalytic systems is primarily explored in environmental applications like water pollutant degradation. Therefore, further exploration of this promising concept in biomedicine, mainly antitumor applications, are needed in the future.

### 3.5. Metal Peroxides-Based Delivery of $H_2O_2$

Metal peroxide-based approaches such as calcium peroxide ($CaO_2$),[45] copper peroxide ($CuO_2$),[46] zinc peroxide ($ZnO_2$),[47] and magnesium peroxide ($MgO_2$)[48] containing systems offer a promising strategy for the treatment of cancer by leveraging the controlled release of $H_2O_2$ in the mild acidic TME using the following equation: "$MO_2 + 2H_2O \rightarrow M(OH)_2 + H_2O_2$."[49] The release of $H_2O_2$ induces oxidative stress selectively in cancer cells, leading to apoptosis, necrosis, and ferroptosis. Besides $H_2O_2$ production ability of metal peroxides, they are able to overcome the challenges of the hypoxic TME by acting as a source for the catalytic generation of $O_2$. This targeted approach enhances the efficacy of cancer treatment by damaging cancerous cells through oxidative mechanisms, potentially overcoming resistance to conventional therapies and minimizing systemic side effects. The application of each metal peroxidase-based delivery of $H_2O_2$ in cancer therapy will be discussed in detail in the following sections.

#### 3.5.1. Calcium Peroxide ($CaO_2$)

Among the various metal peroxides studied for cancer therapy, $CaO_2$ is a versatile and mainly investigated metal peroxide, which exhibited excellent biocompatibility and safety compared to others, as calcium is the most abundant metallic element in the human body (**Table 2**). Moreover, $CaO_2$ can simultaneously produce $O_2$ and $H_2O_2$ under acidic conditions like TME through the following reaction described in Equations (1) and (2) and provide calcium overload to facilitate cell apoptosis via ion-interference therapy.[50]

$$CaO_2 + 2H_2O \rightarrow Ca(OH)_2 + H_2O_2 \uparrow \quad (1)$$

$$CaO_2 + H_2O \rightarrow Ca(OH)_2 + 1/2O_2 \uparrow \quad (2)$$

*Synthesis of $CaO_2$:* The $CaO_2$ NPs are mainly synthesized via the hydrolysis-precipitation technique with some modifications. $CaCl_2$, $CaSO_4$, $CaCO_3$, or $Ca(OH)_2$ as calcium precursors are initially dissolved in alkaline aqueous solutions.[51] Also, to reduce the hydrolysis of $CaO_2$ NPs, ethanol, and methanol have been used instead of an aqueous solution.[52] After the dissolution of calcium salts, $H_2O_2$ is added dropwise to the mixture, followed by stirring until the formation of white $CaO_2$ NPs. Equation (3) shows the overall reaction of agents and the synthesis process involved in preparing $CaO_2$ NPs.

$$CaCl_2 + H_2O_2 + 2NH_4OH \rightarrow CaO_2 + 2NH_4Cl + 2H_2O \quad (3)$$

However, this method has a limitation of aggregated nanoparticles, which can affect their stability, dispersibility, and efficacy in biomedical applications.[53] To overcome this issue, surface stabilizers such as PEG,[51a] PVP,[50a,54] polyvinyl alcohol (PVA),[55] polyacrylic acid (PAA),[56] dextran,[57] starch,[58] and tannic acid (TA)[53a] can be used as surface modifiers for $CaO_2$ particles. Surface stabilizer-coated $CaO_2$ particles can be achieved by synthesizing them directly in the stabilizer medium.[51a]

*$CaO_2$ and Its Role in Cancer Therapy*: $CaO_2$ serves as a pivotal agent in cancer therapy, facilitating the production of $H_2O_2$ and $O_2$ as well as inducing apoptosis through calcification (Table 2).[50b,59]

However, the hypoxic microenvironment of tumors often impairs the efficacy of PDT. To address this challenge, Hu et al. investigated the potential of the $CaO_2$ NPs in PDT for breast cancer treatment, owing to their superior $H_2O_2$ and $O_2$ generating capacity.[45] However, the comparatively slow release of $O_2$ from these NPs hindered the enhancement of PDT efficacy. Therefore, $MnO_2$ was applied as a nanozyme to aid the $O_2$ release from $CaO_2$ (**Figure 4**a). $MnO_2$ shows excellent catalase-like activity with enhanced stability and has been employed to facilitate in situ $O_2$

**Table 2.** Critical paradigms of $CaO_2$-based biomaterials for various cancer treatments.

| Biomaterial | Size | Dose in vitro (cell viability); in vivo | Cancer type | In vitro cell line | In vivo model | Application | Refs. |
|---|---|---|---|---|---|---|---|
| DOX + $CaO_2$/CAT containing alginate pellets | 1.8 mm | 20 pellets $mL^{-1}$ (≈85%); 2 mg $kg^{-1}$ | Lung | Hep3B | Hep3B bearing BALB/c | Chemotherapy | [60] |
| LipoMB/$CaO_2$ liposome | 70 nm | 1.5 μg $mL^{-1}$ (13.3%); 15 mg $kg^{-1}$ of $CaO_2$ | Breast | 4T1 | 4T1-bearing BALB/c | PDT | [61] |
| SA-$CaO_2$ microspheres | 6 μm | 100 μg $mL^{-1}$ of $CaO_2$ (25%); – | Hepatocellular carcinoma | VX2 | VX2 bearing male New Zealand white rabbit; HepG2, H22, and 4T1 bearing BALB/c | Calcification | [59] |
| PMPS-b-P(NIPAAm-co-VBRB) coated $CaO_2$ NPs | 228 nm | – | N/A | – | – | PDT | [62] |
| Ce6 + $CaO_2$ and $MnO_2$ NPs | $CaO_2$ = 300 nm; $MnO_2$ = 3.5 nm | —; 15 mg $kg^{-1}$ of $CaO_2$ and 5 mg $mL^{-1}$ of $MnO_2$ | Breast | 4T1 | 4T1 bearing BALB/c | PDT | [45] |
| HA-$CaO_2$-DOX@MOF-199 NPs (HA-CD@MOF) | 263 nm | 100 μg $mL^{-1}$ (16.4%); 2.8 mg $kg^{-1}$ | Breast | 4T1 | 4T1 bearing BALB/c | CDT/chemotherapy | [63] |
| $CaO_2$@DOX@ZIF-67 nanospheres | 200 nm | 50 μg $mL^{-1}$ (≈20%); 5 mg $kg^{-1}$ | Breast | MCF-7 | MCF-7 bearing Nu/Nu nude mice | CDT/chemotherapy | [64] |
| $CaO_2$/DOX@Cu/ZIF-8@HA NPs (CDZH) | 150 nm | 100 μg $mL^{-1}$ (20%); 1 mg per mouse | Lung | A549 | A549-bearing athymic nude mice | CDT/chemotherapy | [65] |
| $CaO_2$@Mn-PDA NPs | 100 nm | 200 μg $mL^{-1}$ (27%); 10 mg $kg^{-1}$ | Skin melanoma | B16F10, MCF-7 | B16F10 bearing BALB/c | CDT/PTT | [66] |
| ($Cu_2Se$-$CaO_2$)@LA NPs | 108 nm | 50 μg $mL^{-1}$ (≈20%); – | Breast | 4T1 | 4T1 bearing BALB/c | CDT/PTT | [67] |
| $CaO_2$@AuNS@HA-DOX NPs | 346 nm | 100 μg $mL^{-1}$ (10%); 100 μg per mouse | Breast | 4T1 | 4T1 bearing BALB/c | CDT/PTT/ chemotherapy | [68] |
| HPB@$CaO_2$/DOX-PAA NPs | 178 nm | 20 μg $mL^{-1}$ (40%); 16.6 mg $kg^{-1}$ | Colorectal cancer | Caco-2 | HCT116 bearing BALB/c-nu | CDT/PTT/ chemotherapy | [69] |

Abbreviations: $CaO_2$@AuNS: calcium peroxide@gold nanoshells; CAT: catalase; DOX: doxorubicin; HA: hyaluronate acid; HPB: hollow Prussian blue; LA: lauric acid; LipoMB: methylene blue integrated liposome; MOF-199: Cu-based metal-organic framework joined by trimesic acid; PAA: polyacrylic acid; PDA: polydopamine; PMPS-b-P(NIPAAm-co-VBRB): Poly(3-methacryloxypropyl trimethoxysilane)-block-poly(*N*-isopropyl acrylamide-co-vinyl benzyl Rose Bengal; SA: sodium alginate; ZIF-67: zeolitic imidazolate framework-67; ZIF-8: zeolitic imidazolate framework 8.

production from $H_2O_2$ for hypoxia alleviation. The in vitro $O_2$ generation assessment showed a burst release of $O_2$ after exposing $CaO_2$ NPs to the $MnO_2$ nanozyme (Figure 4b). Moreover, the photodynamic singlet oxygen generation with chlorin e6 (Ce6), a type II photosensitizer, was measured using a $^1O_2$ sensor green (SOSG) probe. The addition of the $MnO_2$ nanozyme resulted in a burst $^1O_2$ release in a concentration-dependent manner, providing a positive effect on PDT efficacy enhancement (Figure 4c). Next, the impact of $CaO_2$/$MnO_2$ on hypoxia regulation was analyzed in 4T1 cells using $[Ru(dpp)_3]Cl_2$ as an oxygen probe. The red fluorescence completely disappeared in the $CaO_2$/$MnO_2$ group, which verified the outstanding ability of $CaO_2$/$MnO_2$ in hypoxia modulation (Figure 4d). Furthermore, the $^1O_2$ generation of $CaO_2$ or $CaO_2$/$MnO_2$ with Ce6 under NIR irradiation was examined in 4T1 cells using the DHR-123 probe. Remarkably, cells treated with Ce6, $CaO_2$/$MnO_2$, and NIR irradiation displayed a 12-fold increase in green fluorescence that highlights the critical role of the $MnO_2$ in providing an accelerated and sufficient $O_2$ supply, thereby enhancing $^1O_2$ production (Figure 4e). Moreover, $MnO_2$ nanozyme could act as a promising magnetic resonance imaging (MRI) T1 contrast agent for image-guided PDT. The maximized MRI enhancement was observed at 6 h post-injection, demonstrating the highest accumulation of $MnO_2$ (Figure 4f). The PDT effect was evaluated in 4T1-injected BALB/c mice under irradiation with a 660 nm NIR laser (0.5 W $cm^{-2}$) for 5 min. At the end of the experiment, a considerable decrease in the tumor volume was observed after treatment with Ce6 with $CaO_2$ (Figure 4g). Hematoxylin and eosin (H&E) and terminal deoxynucleotidyl transferase dUTP nick-end labeling (TUNEL) staining analysis of tumor tissue slides showed significant necrosis and apoptosis in the Ce6+$CaO_2$/$MnO_2$ treated group, which can confirm the importance of effective hypoxia relief in PDT efficacy enhancement (Figure 4h). Moreover, the expression of HIF-1$\alpha$ and vascular endothelial growth factor (VEGF), two upregulated factors in hypoxic tumor environments, were significantly decreased after $CaO_2$/$MnO_2$ treatment, reducing resistance associated with hypoxia and preventing tumor recurrence and metastasis (Figure 4i).

Similarly, Han et al. investigated a novel nanotheranostic platform by engineering $CaO_2$ and $Fe_3O_4$ hybrid NPs with hyaluronate acid (HA) stabilizer and NIR fluorophore label for cancer therapy and bimodal imaging.[70] The prepared system showed a high capacity for self-supply of $H_2O_2$ and production of •OH in acidic conditions with excellent stability in physiological conditions. It showed high selectivity for 4T1 tumor cells through CDT with minimal toxicity for normal cells (NIH/3T3

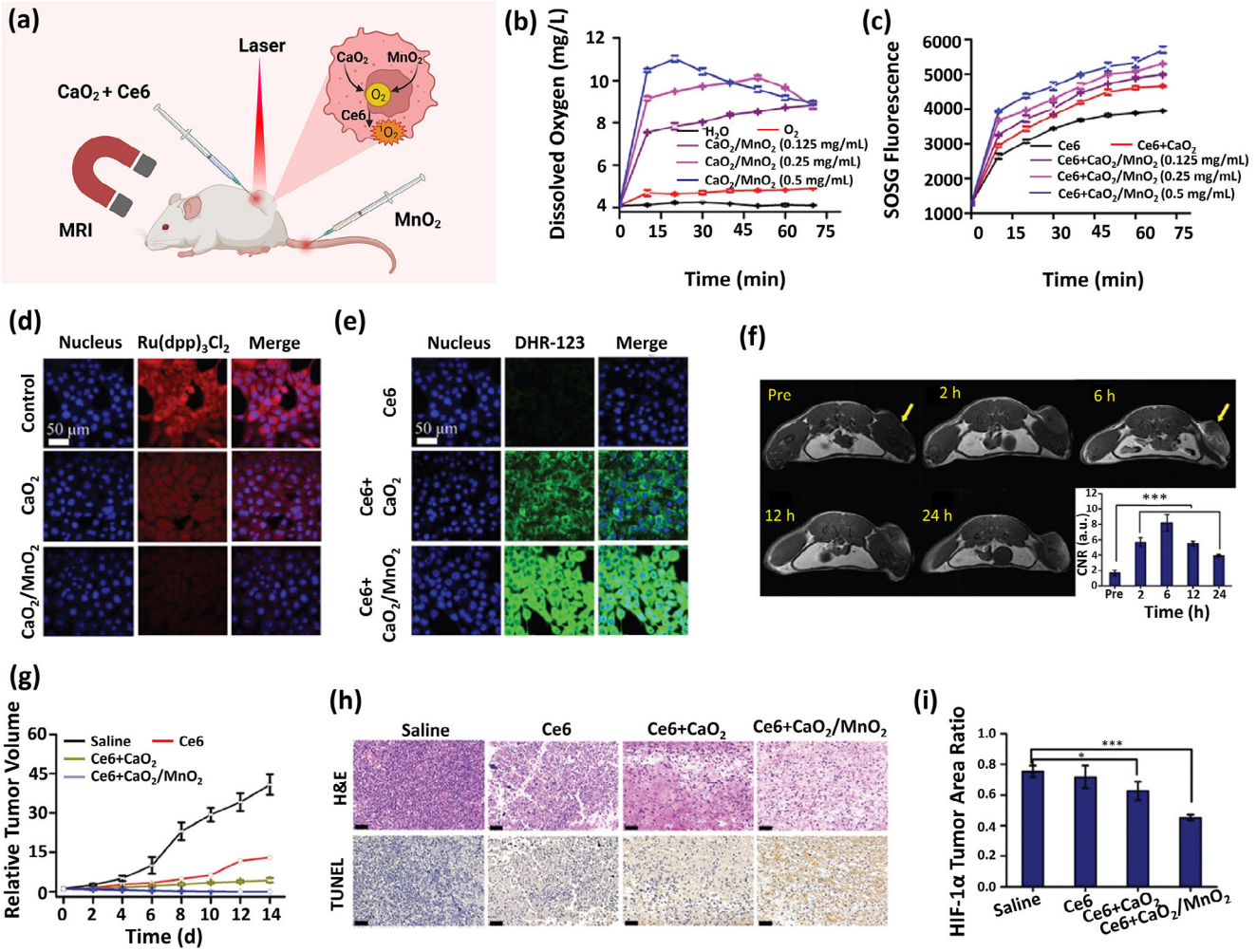


**Figure 4.** a) Schematic illustration of $CaO_2$ NPs catalyzed by $MnO_2$ for $O_2$ release for hypoxia modulation and MRI-guided PDT. Created on Biorender. b) $O_2$ generation of $CaO_2$ NPs (0.5 mg $mL^{-1}$) in combination with $MnO_2$ NPs at different concentrations ($N = 3$). c) Photodynamic $O_2$ release of $CaO_2$ NPs (0.5 mg $mL^{-1}$) with Ce6 and $MnO_2$ nanozyme at different concentrations under 660 nm NIR laser (20 mW $cm^{-2}$) irradiation ($N = 3$). d) Confocal laser scanning microscopy (CLSM) images of 4T1 cells treated with $[Ru(dpp)_3]Cl_2$ after 6 h incubation with NPs. e) CLSM images of 4T1 cells treated with DHR-123 after 4 h incubation with different NPs, subsequently irradiated by 660 nm NIR laser (20 mW $cm^{-2}$, 1 min). f) In vivo MRI T1 images of mice bearing 4T1 tumors before and after injection of $MnO_2$ NPs and complementary CNR analysis ($N = 5$, $^{***}p < 0.001$). g) Changes in the relative tumor volume after different PDT treatments ($N = 5$). h) TUNEL and H&E staining of tumor sections from different experimental groups (scale bar = 50 μm). i) Quantitative analysis of HIF-1α ($^{*}p < 0.05$ and $^{***}p < 0.001$). Reproduced with permission.[45] Copyright 2020, Royal Society of Chemistry.

and LO2 cell lines) in in vitro studies. Also, in vivo studies exhibited that this nanotherapeutic agent effectively inhibited tumor growth through CDT with a tumor growth inhibition rate of 69% compared to the control group. In addition, dual-modality NIR fluorescence (NIRF) and MRI demonstrated tumor-specific targeting and treatment, allowing visualization of the CDT process. These findings confirmed the potential of the active targeting, $H_2O_2$ self-supplying, and bimodal imaging nanotheranostic platform as a potent strategy for CDT for cancer treatment.

As a versatile material, $CaO_2$ has multifunctional properties that contribute to various cancer therapies, making it a promising candidate for combination therapies. Incorporation of $CaO_2$ into treatments such as chemotherapy, PDT, CDT, and immunotherapy have been shown to increase their effectiveness significantly.[64,71] To further investigate the potential of $CaO_2$ in combinatorial therapies, we first explore its integration with DOX. This chemotherapeutic agent activates NOXs that can transform $O_2$ into ROS and cause ROS overproduction inside mitochondria, promoting cell death and enhancing therapeutic efficacy against cancer cells.[72] Du et al. prepared a self-reinforced bimetallic therapeutic system by offering HA-modified DOX, $CaO_2$, and copper MOF integrated platform (HA-CD@MOF NPs) to boost cuproptosis/immunotherapy outcome in anti-cancer studies (**Figure 5a**).[63] The HA provides excellent targeting of CD44-positive tumor cells and minimizes side effects, while the release of DOX and $CaO_2$ exacerbates ROS production and mitochondrial damage, enhancing the overall therapeutic effect. These NPs showed a notable increase in the production of $H_2O_2$ over time in the presence of hyaluronidase (HAD) and GSH (Figure 5b), strengthening the $Cu^{2+}$-based Fenton-like reaction for CDT. Flow cytometry analysis revealed that the highest apoptotic rate of 4T1 cells belongs to the HA-CD@MOF

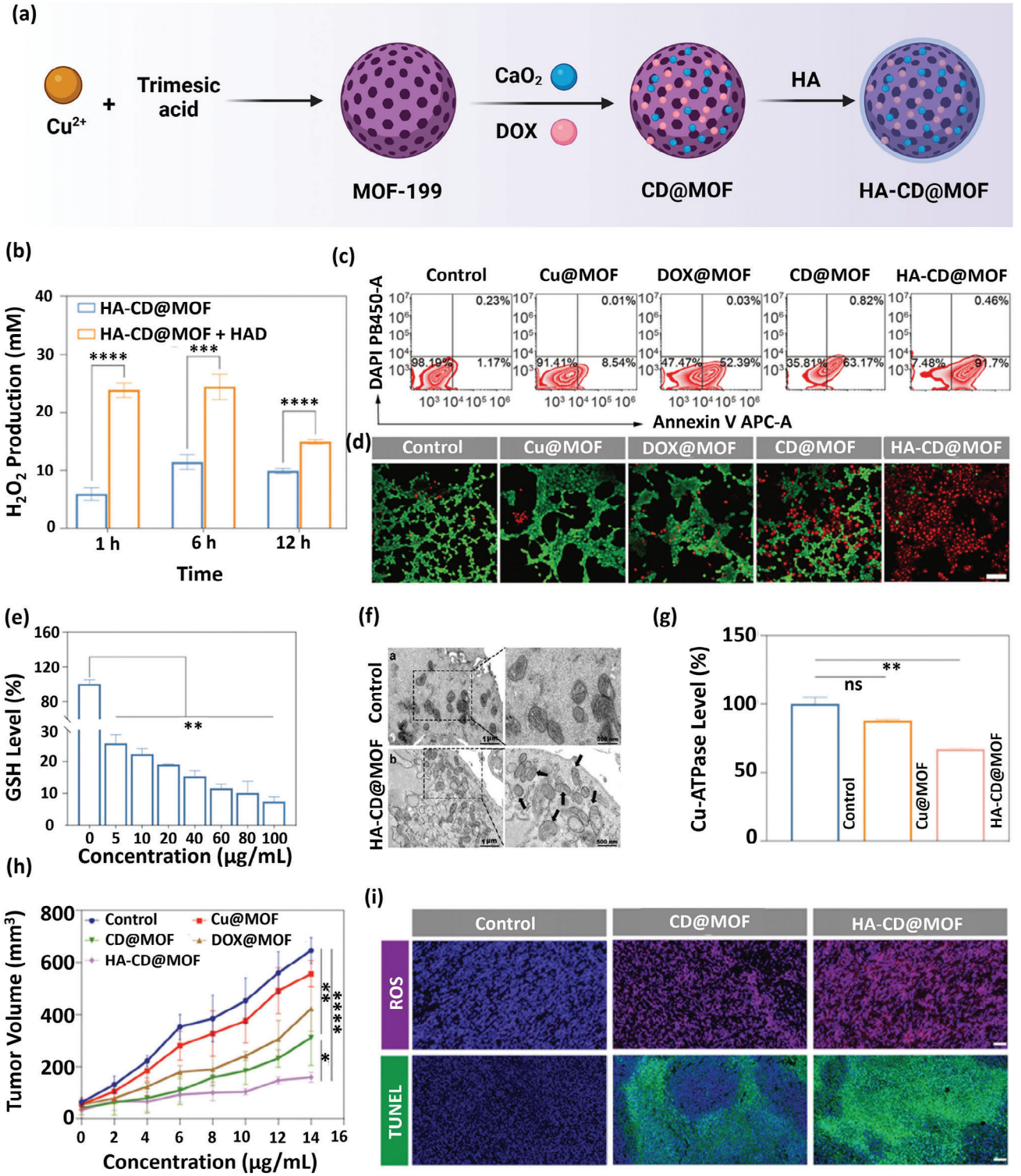


**Figure 5.** a) Schematic illustration of the HA-CD@MOF NPs synthesis. Created on Biorender.com. b) $H_2O_2$-generation of the HA-CD@MOF NPs in the presence or absence of HAD in solutions containing GSH (10 mm, $N = 3$). c) FCM measurement of 4T1 cell apoptosis ratios in different groups. d) CLSM images of live and dead stained 4T1 cells after treatment with various MOFs. Red fluorescence represents dead cells, and green fluorescence represents live cells (scale bar: 50 μm). e) GSH depleting function of the HA-CD@MOF NPs with different concentrations ($N = 3$). f) Bio-TEM of mitochondria in control and HA-CD@MOF NP-treated 4T1 cells. g) Cu-ATPase activity after different treatments ($N = 3$). h) Tumor volume of tumor-bearing mice after various treatments ($N = 5$). i) ROS and terminal deoxynucleotidyl transferase dUTP nick-end labeling (TUNEL) staining of tumor tissues (scale bars: 100 μm). Results are presented as means ± SD. $^*p < 0.05$, $^{**}p < 0.01$, $^{***}p < 0.001$, $^{****}p < 0.0001$. Reproduced with permission.[63] Copyright 2024, Wiley.

group, reaching up to 91.7% (Figure 5c). Further assessment using calcein-AM and propidium iodide staining demonstrated that HA-CD@MOF significantly increased the number of dead cells compared to other groups, indicating the efficacy of bimetallic ions in tumor elimination (Figure 5d). Besides CDT, cuproptosis-dependent cell death is another implemented approach in this study to kill tumor cells, which can be confirmed by mitochondrial damage. This damage can be impeded by the presence of the copper transporter family and the elevated expression of GSH and in cancer cells. HA-CD@MOF presented a significant reduction in GSH levels (Figure 5e) as well as a swollen morphology of the mitochondria (Figure 5f) and a reduction of the $Cu^{2+}$ efflux ability of Cu-ATPase (Figure 5g), leading to cuproptosis sensitization. Furthermore, in vivo studies demonstrated the considerable therapeutic effect of HA-CD@MOF-treated 4T1 tumor-bearing mice in tumor suppression (Figure 5h). As shown in Figure 5i, immunofluorescence staining and TUNEL of the tumor tissues exhibited the highest accumulation of ROS (red) and the highest apoptotic rate (green spot), respectively, in the HA-CD@MOF-treated group. Furthermore, the ability of the HA-CD@MOF system to induce immune cell death and inhibit metastasis indicates its potential as a comprehensive approach for boosting tumor cuproptosis and immunotherapy.

In another study, the $CaO_2$@DOX@ZIF-67 system was prepared to improve chemo/chemodynamic therapy through a bottom-up approach.[64] This nanocatalytic system was designed to deliver $O_2$ and $H_2O_2$ to the tumor tissue simultaneously. In the weakly acidic environment of tumors, $CaO_2$@DOX@ZIF-67 decomposes to release $Co^{2+}$, a Fenton-like catalyst, and the DOX as a chemotherapeutic drug. Unprotected $CaO_2$ reacts with water to produce $O_2$ and $H_2O_2$. The released $O_2$ helps reduce tumor hypoxia, thereby improving the efficacy of DOX. At the same time, $H_2O_2$ reacts with $Co^{2+}$ to generate highly toxic $^{\bullet}OH$ through a Fenton-like reaction, thereby enhancing dynamic chemotherapeutics. Both in vitro and in vivo results showed that $CaO_2$@DOX@ZIF-67 exhibits excellent antitumor activity with low systemic toxicity, which makes it a promising candidate for combined chemotherapy and pH-responsive CDT.

Combining PTT with CDT offers a powerful synergistic approach for cancer treatment by increasing the efficiency of the Fenton reaction by temperature elevation and alleviating tumor hypoxia by improving the blood flow.[73] Specifically, in recent years, a combination of PTT with $CaO_2$-based nanomedicines has revealed significant antitumor effects by a targeted cancer therapy approach.[74] In this line, Feng et al. introduced a novel nanocomposite (($Cu_2Se$-$CaO_2$)@LA) that uses near-infrared (NIR) radiation to enhance CDT effects.[67] NIR radiation melts a lauric acid coating, exposing $CaO_2$ NPs, which react with water to produce $H_2O_2$. Further, $Cu_2Se$ showed higher $^{\bullet}OH$ production from $H_2O_2$ in higher temperatures, indicating the influence of hyperthermia in enhancing the outcome of the CDT. In addition, this process enhances immune responses by increasing ROS, increasing dendritic cell maturation, recruiting cytotoxic T cells, and ultimately suppressing tumor growth. Therefore, this approach offers a promising strategy to enhance immunogenic death (ICD) and improve the efficacy of tumor immunotherapy.

Expanding on the synergy between CDT and PTT, a recent study by Wang et al. explored the combination of CDT, PTT, and chemotherapy for cancer treatment.[68] The DOX-loaded HA-coated core NPs ($CaO_2$@Au nanoshells) were designed as a synergistic platform for self-supplying of $H_2O_2$ and NIR-enhanced ROS production for CDT-PTTs-chemotherapy multimode drug delivery (**Figure 6a**). The in situ deposited gold nanoshells not only provide effective photothermal treatment, which increased temperature by 25 °C within 5 min after exposure to 808 nm laser, but also act as peroxidase mimetics and catalyze $H_2O_2$ to $^{\bullet}OH$ for potent CDT (Figure 6b). The $CaO_2$@AuNS@HA-DOX nanoplatform showed higher ROS generation at pH 5 as compared to pH 7, indicating its sensitivity in acidic environments. This pH-sensitive ROS generation, concurrently with the stability of the nanoplatform at physiological pH, ensures low toxicity to normal cells while being more cytotoxic in the acidic TME. Under NIR irradiation, the increased local temperature loosens HA's thermosensitive structure and exposes $CaO_2$ to an acidic environment, causing ROS generation. In addition, the presence of hyaluronidase (HAase) in TME accelerates the generation of ROS by degrading HA (Figure 6c). Therefore, acidic pH, NIR irradiation, and the presence of HAase increase the release of DOX from the $CaO_2$@AuNS@HA-DOX (Figure 6d). Moreover, in vitro and in vivo studies demonstrated the improved tumor therapy of the $CaO_2$@AuNS@HA-DOX+NIR group through the synergistic therapy of enhanced CDT, PTT, and chemotherapy against breast cancer (Figure 6e–g).

Complementing the advances in CDT, PTT, and chemo- and immune-therapy have also emerged as a significant strategy in cancer treatment. Immunotherapy combined with the generation of ROS through PDT based on $CaO_2$ NPs can trigger immunogenic cell death to treat cancer effectively.[75] Considering the synergistic effect of CDT and immunotherapy in cancer therapy, Qian et al. developed MIL-101(Fe) loaded with ultrafine Cu NPs, Pt, and indoleamine 2,3-dioxygenase (IDO) inhibitor 1-methyl-D-tryptophan (1-MT) and further coated with 5,10,15,20-tetrakis(4 carboxyphenyl)porphyrin (TCPP) photosensitizer, PDA, and $CaO_2$ as a new nanoplatform (Cu@MIL-101@PMTPC).[76] This nanoplatform enhances CDT through both Fenton and Fenton-like reaction facilitated by $Fe^{3+}$ in MIL-101(Fe) and copper NPs. The IDO inhibitor 1-MT helps to overcome chemotherapy-induced immune escape, enhancing the immune response of T cells. Moreover, the toxic side effects of chemotherapy can be decreased by the acid-induced release of both drugs in TME. In addition, TCPP generates $^1O_2$ when laser irradiated to kill tumor cells, while $CaO_2$ reduces tumor hypoxia by generating $O_2$ and $H_2O_2$, further enhancing PDT and providing a continuous supply of $H_2O_2$ to the Fenton-like reaction. The reaction of this multifunctional nanoplatform demonstrates a powerful integration of CD, PD, and immunotherapy and provides a promising new strategy for effective cancer treatment.

Consequently, $CaO_2$ has shown great promise in cancer treatment, both as a monotherapy and in combination therapies, due to its ability in calcification, generate $H_2O_2$, and enhance the activity of nanocatalysts.[59,69] However, to fully realize its potential in clinical applications, further research is necessary to increase its stability, selectivity, and optimization of its nanoformulation. Addressing these challenges will be essential for the successful development of $CaO_2$-based therapies in cancer treatment.

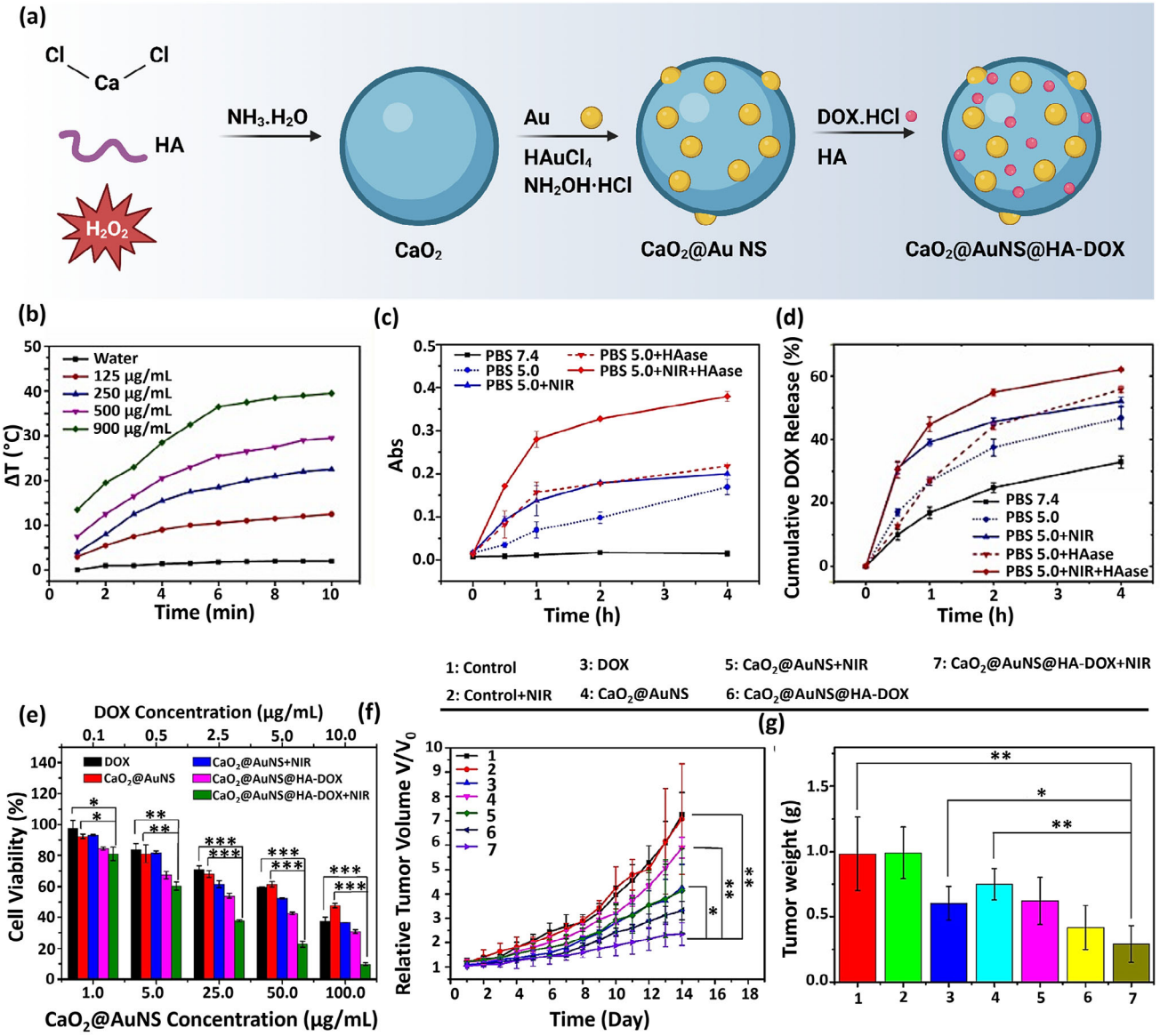


**Figure 6.** a) Schematic illustration of the preparation of $CaO_2$@AuNS@HA-DOX system for synergistic CDT-PTT-chemotherapy. Created on Biorender.com. b) Photothermal effect of $CaO_2$@AuNS@HA-DOX under the NIR laser irradiation (2.0 W $cm^{-2}$) in different concentrations over 10 min. c) The ROS production of $CaO_2$@AuNS@HA-DOX under different conditions. d) DOX release profiles of $CaO_2$@AuNS@HA-DOX under different conditions. Data were presented as mean ± SD ($N = 3$). e) The viability of 4T1 cells after incubation with components of the $CaO_2$@AuNS@HA-DOX system for 24 h at 37 °C with or without NIR irradiation (1.5 W $cm^{-2}$, 5 min). Data were presented as mean ± SD ($N = 5$). f) Relative tumor volume curves. g) Tumor weights of different groups. ***$p < 0.001$, **$p < 0.01$, *$p < 0.05$. Reproduced with permission.[68] Copyright 2022, Elsevier B.V.

### 3.5.2. Copper Peroxide ($CuO_2$)

Among metal ions that can induce Fenton/Fenton-like reactions, copper has advantages, like a broader pH range to produce •OH, excellent GSH depletion rate, and fast conversion of $Cu^{2+}$ to $Cu^{+}$.[77] Consequently, using copper in a peroxide compound to synthesize $CuO_2$ NPs will benefit from the advantages of using copper in an $H_2O_2$ self-supplied system. The NPs in the presence of acid could release $Cu^{2+}$, which can be consumed by antioxidants like GSH in TME and become reduced to $Cu^{+}$.[78] This $Cu^{+}$ has the potential to become oxidized in the presence of self-reinforced $H_2O_2$ and produce •OH and $Cu^{2+}$, completing the cycle of $Cu^{2+}/Cu^{+}$. Thus, $CuO_2$ NPs disrupt the oxidative redox of cancerous cells, which can lead to efficient and targeted anticancer treatment.

*Synthesis of the $CuO_2$ NPs*: The catalytic $CuO_2$ NPs with the aim of producing $H_2O_2$ and $Cu^{2+}$ were broadly studied and synthesized with dissolving Cu salts in the aqueous solution of different stabilizers like PVP,[79] dextran,[80] human serum albumin (HSA).[81] Then, after adjusting the pH with NaOH, the $H_2O_2$ is added dropwise to synthesize $CuO_2$ NPs, which is represented in Equation (4).

$$CuCl_2 + H_2O_2 + 2NaOH \rightarrow CuO_2 + 2NaCl + 2H_2O \quad (4)$$

**Table 3.** Critical paradigms of $CuO_2$-based biomaterials for various cancer treatments.

| Biomaterial | Size | Dose in vitro (cell viability); in vivo | Cancer type | In vitro cell line | In vivo model | Application | Refs. |
|---|---|---|---|---|---|---|---|
| $CuO_2$-MSN@TA-$Cu^{2+}$ NPs | 100 nm | 200 μg $mL^{-1}$ of MSN (≈10%); 20 mg $kg^{-1}$ of MSN | Breast | 4T1 | 4T1 bearing BALB/c | CDT | [82] |
| $CuO_2$/ZIF-8//polydopamine | 200 nm | – | – | – | – | CDT | [79a] |
| LIPSe@$CuO_2$&DHA liposome | 80–90 nm | 200 μg $mL^{-1}$ of LIP (≈15%); 10 mg $kg^{-1}$ of LIPSe | Breast | 4T1 | 4T1 bearing BALB/c | CDT | [24a] |
| PLGA@carbon quantum dots–$CuO_2$ NPs | 150 nm | 80 μg $mL^{-1}$ (≈10%); – | Breast | MDA-MB-468 | – | CDT | [21a] |
| $CuO_2$-PVP-SRF NPs | 187 nm | 100 μg $mL^{-1}$ (≈7%); – | Breast | 4T1 | – | CDT | [79b] |
| HES-DOX stabilized $CuO_2$ NPs integrated with SSZ (HSCPs) | 191 nm | 10 μg $mL^{-1}$ of DOX (≈7%); 3 mg $kg^{-1}$ | Breast | 4T1 | 4T1 bearing mice | CDT/Chemotherapy | [83] |
| $CuO_2$@PEG-DSF NPs | 100 nm | 0.3 μg $mL^{-1}$ of $CuO_2$ (<10% in both cell lines); 0.175 mg $kg^{-1}$ | Lung; Breast | A549; 4T1 | 4T1 bearing BALB/c | CDT/Chemotherapy | [84] |
| $CuO_2$/cisplatin@$SiO_2$ NPs | 100 nm | 5 μM of cisplatin (≈15%); 1 mg $kg^{-1}$ of cisplatin | Liver | H22 | H22 bearing BALB/c | CDT/chemotherapy | [85] |
| UCN@$CuO_2$–GOx nanocomposite | 25 nm | 6.3 μg $mL^{-1}$ (≈6%); – | Cervical | HeLa | – | CDT/ST | [86] |
| HSA-Ce6-$CuO_2$ NPs | 45 nm | 40 μg $mL^{-1}$ of $CuO_2$ (≈10%); 3 mg $kg^{-1}$ of $CuO_2$ | Breast | 4T1 | 4T1 bearing BALB/c | CDT/PDT | [81] |
| DSF/Ce6@ZIF-8@$CuO_2$ NPs | 106 nm | 50 μg $mL^{-1}$ (≈14%); 20 mg $kg^{-1}$ | Breast | 4T1 | 4T1 bearing BALB/c | CDT/PDT | [87] |
| TMB-$CuO_2$@PLGA@ red blood cell membrane NPs | 125 nm | 150 μg $mL^{-1}$ (≈30%); 4 mg $kg^{-1}$ | Breast | 4T1 | 4T1 bearing BALB/c | CDT/PTT/PAI | [46] |
| $CuO_2$/Mn-Prussian blue NPs | 464 nm | – | Gastric | SGC-7901 | – | CDT/PTT/Biosensing | [79c] |
| $CuO_2$ NPs and DSF encapsulated microneedles | $CuO_2$ NPs = 10 nm | – | Melanoma | B16F10 | B16F10 bearing BALB/c | CDT/PTT/ chemotherapy | [88] |
| DOX/MCN-$CuO_2$-HA | 120 nm | 100 μg $mL^{-1}$ (≈13%); 200 μg per mouse | Breast | 4T1 | 4T1 bearing BALB/c | CDT/PTT/ chemotherapy | [89] |

Abbreviations: Ce6: Chorin-e6; DHA: dihydroartemisinin; DOX: doxorubicin; DSF: disulfiram; HA: hyaluronic acid; HES: hydroxyethyl starch; HSA: human serum albumin; LIPSe: liposome; MCN: mesoporous carbon nanospheres; MSN: mesoporous silica nanoparticles; PLGA: poly lactic-co-glycolic acid; SSZ: sulfasalazine; TA: tannic acid; TMB: 3,3′,5,5′-Tetramethylbenzidine; SRF: sorafenib; UCN: upconversion NPs; ZIF-8: zeolitic imidazolate framework 8.

*$CuO_2$ and Its Role in Cancer Therapy*: Owing to the high Fenton activity and $H_2O_2$ self-supply of $CuO_2$, the effect of these metal peroxides has been widely investigated for tumor therapy purposes (**Table 3**).

Chen et al. designed a sorafenib (SRF)-loaded $CuO_2$ NPs that stabilized by PVP to enhance the CDT outcome in the acidic pH of the tumor environment.[79b] Besides the in situ enhanced Fenton-like reaction by $H_2O_2$ and $Cu^{2+}$, released SRF can disrupt the redox balance by hindering the activity of system $xc^-$. System $xc^-$ is a cystine-glutamate exchange transporter in the membrane, transporting the glutamate outside of cells and exchanging it with extracellular cystine, which is the precursor of the antioxidant GSH.[90] So, by terminating the function of the system $xc^-$, the production rate of the GSH can be reduced. Due to these strategies, the synthesized $CuO_2$-PVP-SRF NPs were detected to destroy 45.5% of 4T1 cancer cells, presenting more efficient cancer cell killing ability in comparison to $CuO_2$-PVP and SRF groups which were 21% and 33.9%, respectively. The disruption in the antioxidant system of the tumor cells, simultaneously with stimulation of the Fenton-like reaction and $H_2O_2$ self-generation, caused cell apoptosis/ferroptosis by lipid peroxidation (LPO) accumulation. In another study, a liposomal system was developed for the co-delivery of $CuO_2$ NPs and dihydroartemisinin (DHA) (LIPSe@$CuO_2$&DHA) to generate lethal ROS for cancer therapy purposes (**Figure 7a**).[24a] Intracellular ROS level studies showed that compared to the control group, 2632% of DCFH-DA fluorescence intensity was found in the cells treated with the LIPSe@$CuO_2$&DHA, suggesting this platform is a great nanocatalytic medicine (Figure 7b). This remarkable ability of the LIPSe@$CuO_2$&DHA in ROS production, besides $Cu^{2+}$-induced GSH depletion (Figure 7c), resulted in disrupted cellular redox balance and ferroptosis-induced cell death. In another study, PLGA-coated carbon quantum dots (CQDs), and copper peroxide NPs (PLGA@CQDs–CuPox NPs) were synthesized through an emulsion-solvent evaporation method for diagnosis and treatment of cancer based on the fluorescence performance of CQDs and CDT of $CuO_2$ NPs.[21a] PLGA was used to improve the EPR effects of both $CuO_2$ and CQDs, hindering the early excretion of the NPs from the body before reaching the tumor site. PLGA@CQDs–CuPox NPs emitted strong green

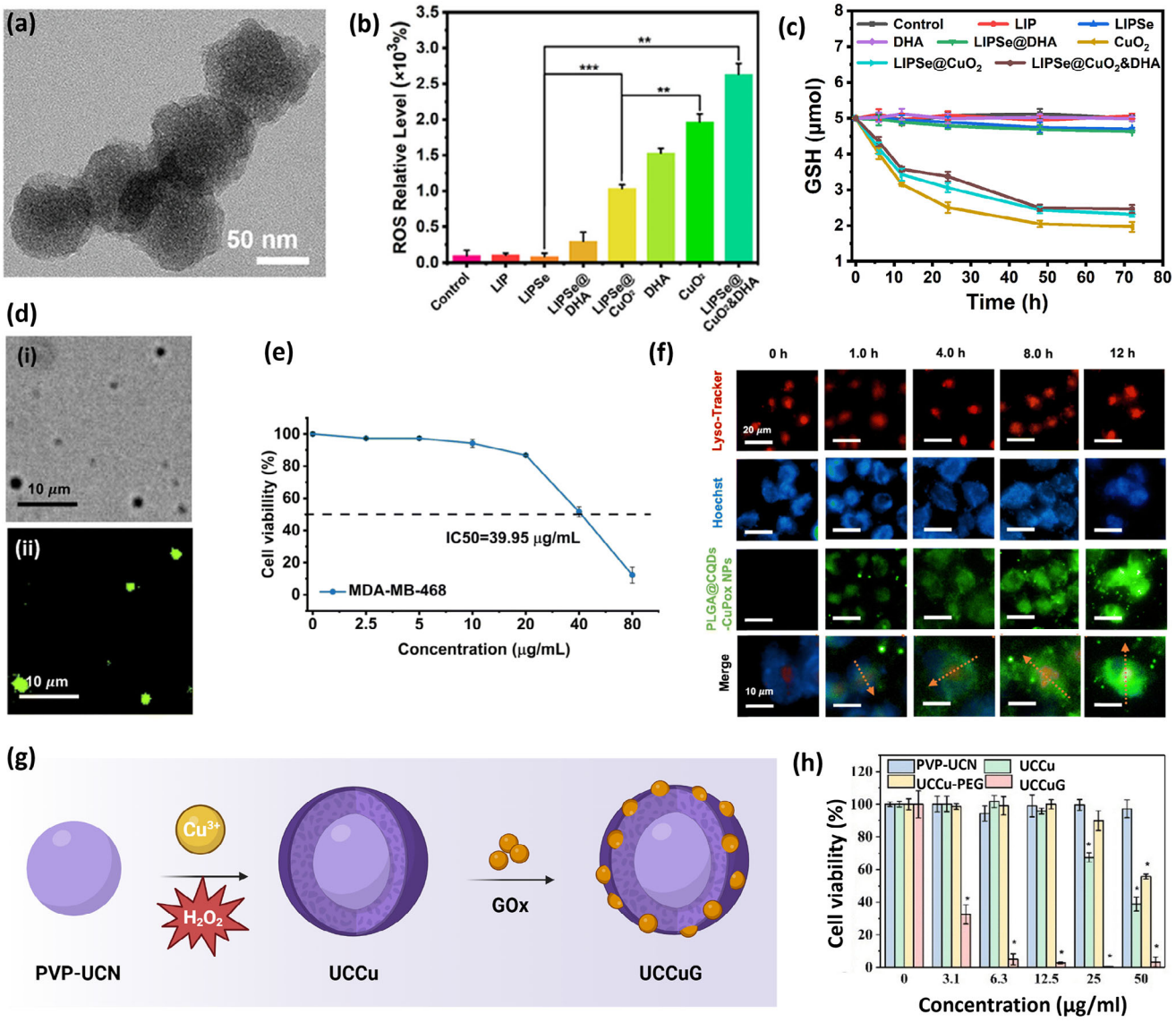


**Figure 7.** a) TEM image of LIPSe@$CuO_2$&DHA. b) Flow cytometric results of DCFH-DA fluorescence in the 4T1 cells treated with different samples. c) The residual GSH amount in aqueous solutions was treated with different samples. Reproduced with permission.[24a] Copyright 2023, American Chemical Society. d) The optical images of PLGA@CQDs–CuPox NPs: i) bright-field image and ii) fluorescence image. e) IC50 values of breast cancer cells treated with different concentrations of PLGA@CQDs–CuPox NPs ($n = 3$). f) CLSM images taken at 0, 1, 4, and 12 h after treatment with PLGA@CQDs–CuPox NPs. Reproduced with permission.[21a] Copyright 2024, Royal Society of Chemistry. g) Schematic illustration of the UCCuG nanocomposite synthetic procedure. Created on Biorender.com. h) Cell viability of HeLa cells treated with different nanocomposites at different concentrations for 24 h. Data are presented as means ± SD ($n = 3$), *$p < 0.05$. Reproduced with permission.[86] Copyright 2022, Royal Society of Chemistry.

fluorescence under excitation of 390 to 420 nm, suggesting a great tool for tracking the NPs accumulation area (Figure 7d). The anti-tumor behavior of the designed system was indicated by 85% of the MDA-MB-468 human breast cancer cells died with 80 μg $mL^{-1}$ of the PLGA@CQDs–CuPox NPs in 24 h (Figure 7e). CLSM of MDA-MB-468 breast cancer cells showed excellent EPR effect by the gradual spread of the NPs throughout the entire cell nuclei and subsequently permeating the entire cell, potentially escaping from the lysosomes in the first hours of treatment (Figure 7f). Cell nuclei emitted blue fluorescence, while lysosomes emitted red fluorescence. Therefore, the designed platform offered a novel approach in cancer theranostics applications utilizing CDT and fluorescence-guided imaging. With a different approach, Hong et al. succeed in coating $CuO_2$ and GOx on the surface of upconversion NPs (UCN) to benefit from ST and CDT simultaneously (Figure 7g).[86] In this study, for monitoring real-time tumor therapeutic ability, lanthanide-doped upconversion NPs were selected to act as a core, which is an excellent candidate for deep tissue fluorescence imaging due to the deep penetration of NIR light in biological tissues. These NPs, according to the anti-Stokes law, have the ability to absorb two or more low-energy photons from the NIR region and emit one

high-energy photon.[91] Therefore, UCN@$CuO_2$-GOx (UCCuG) was developed to produce excess $H_2O_2$ and gluconic acid in the TME by both GOx and $CuO_2$, which can be catalyzed by $Cu^+$ to free hydroxyl radicals. In vitro cytotoxicity experiments on the HeLa cells displayed that the UCCuG group has the highest toxicity among other groups, suggesting the power of the combination therapy compared to each treatment alone (Figure 7h). Additionally, the core was able to make upconversion luminescence in 980 nm for bioimaging, which is a great function for real-time in vivo monitoring. Therefore, this designed platform is suggested to be exploited for starvation-enhanced CDT for tumor therapy.

The $CuO_2$ NPs have been used with other treatment modalities, including chemotherapy, PTT, and PDT, to achieve more effective tumor eradication. Focusing on combining the CDT and chemotherapy, He et al. loaded $CuO_2$ and cisplatin (DDP) in silica NPs to synthesize $CuO_2$/DDP@$SiO_2$ NPs (**Figure** 8a).[85] The more interesting section of this study was revealed when the $CuO_2$ significantly increased the cisplatin sensitization in both in vitro and in vivo studies. In vitro experiments on H22 cells exhibited that this approach improves the anti-tumor effect by activating the caspase-related apoptotic pathways by cisplatin (Figure 8b) as well as remodeling TME by alleviating acidosis, hypoxia, and high GSH levels in the TME by $CuO_2$ NPs. (Figure 8c–e). GSH depletion allows cisplatin accumulation inside tumor cells without binding to GSH as a cisplatin-efflux pathway. It was also noteworthy that the $CuO_2$/DDP@$SiO_2$ group exhibited an excellent level of ROS production due to the stimulation of the Fenton-like reaction by Cu ions and the capacity of the cisplatin to produce ROS (Figure 8f). Thus, combining $CuO_2$ with cisplatin suggested a promising approach in showing synergistic antitumor effects. In another attempt, $CuO_2$ NPs again affirmed their capacity to enhance the antitumor effect of a chemotherapeutic drug called disulfiram (DSF), which is a brand-new agent that, in its usage in clinics, suffers from poor stability.[92] However, the chelation product of DSF with $Cu^{2+}$ (CuET) can address this by designing a codelivery system of $Cu^{2+}$ and DSF. As such DSF and Ce6, a photosensitizer, were encapsulated in zeolite imidazole framework-8 (ZIF-8), followed by loading of HA stabilized $CuO_2$ on the surface of DSF/Ce6@ZIF-8 to develop DSF/Ce6@ZIF-8@$CuO_2$ (DCZCu) for chemotherapy/CDT/PDT (Figure 8g).[87] After active targeting of HA-modified nanocarrier to overexpressed CD44 on the surface of the cancer cells, the acidic condition of TME led to the production of CuET as well as the enhanced release of $H_2O_2$ and $O_2$. In vitro and in vivo studies exhibited that the DCZCu treated group has the highest $H_2O_2$ production (Figure 8h), GSH degradation rate (Figure 8i), ROS generation (Figure 8j), and anticancer cell death ability among other groups, indicating the potential effect of synergistic treatment. Moreover, intending to enhance physiological stability and tumor enrichment as well as extend the circulation half-life, Xiong et al. suggested the synthesis of the sulfasalazine-integrated hydroxyethyl starch-DOX conjugate-stabilized $CuO_2$ NPs (HSCPs) and compare them with PVP-stabilized $CuO_2$ NPs in terms of physiological stability, blood half-life, and tumor enrichment.[83] Specifically, in this study, hydroxyethyl starch was loaded by DOX and used as a stabilizer. The sulfasalazine and $CuCl_2$ were added to the mixture before adding the NaOH and $H_2O_2$. To evaluate the physiological stability, the hydrodynamic size distribution of the HSCPs was monitored in different media, and it was constant for four weeks, suggesting the excellent stability of the NPs (Figure 8k). Also, synthesized HSCPs showed 3.19 h of blood half-life time, which was higher than the PVP-$CuO_2$ (0.77 h) (Figure 8l). Furthermore, PVP-$CuO_2$ represented significantly less tumor accumulation, which was 0.57 times that of HSCPs (Figure 8m).

Among these synergistic treatment approaches, integrating CDT and PDT using $CuO_2$ NPs presents a potent treatment for intensified oxidative damage to cancer cells. To this end, human serum albumin (HSA) was utilized as a stabilizer for $CuO_2$ NPs and also a connector for chlorin e6 (Ce6), which is an $O_2$ supplier in this platform, improving the outcome of CDT- and PDT-mediated combination cancer therapy.[81] After disintegrating in the tumor's acidic environment, this platform enhanced the concentration of the highly toxic hydroxyl radicals by increasing the concentration of the $H_2O_2$ and releasing $Cu^{2+}$ to catalyze the Fenton-like reaction for highly efficient CDT. Also, this $H_2O_2$ can be decomposed to $O_2$, improving the outcome of PDT. In vitro cytotoxicity tests on 4T1 cells were also conducted and indicated that the HSA-Ce6-$CuO_2$ treated group with 660 nm laser irradiation for 3 min had the highest cytotoxicity rate (**Figure** 9a). Flow cytometry results displayed that the HSA-Ce6-$CuO_2$ treated group with laser irradiation has the highest apoptotic cell ratio compared to the exact group without laser irradiation ($p < 0.001$) (Figure 9b). In vivo studies also proved the results of in vitro experiments, suggesting the great potential of ROS generation from a Fenton-like reaction and hypoxia relief (Figure 9c). Furthermore, a combination of the PTT with $CuO_2$-induced CDT can cause local hyperthermia, which not only disrupts tumor cells but also can enhance the generation of the $H_2O_2$ from $CuO_2$. Accordingly, $CuO_2$ NPs and 3,3′,5,5′-tetramethylbenzidine (TMB) were coloaded into poly(lactic-co-glycolic acid) (PLGA), which was subsequently camouflaged by red blood cell membrane to achieve TCPR NPs for in vivo TME-activated photoacoustic imaging (PAI)/PTT/CDT theranostics (Figure 9d).[46] Red blood cell membranes were used to enhance the blood circulation time, permeability, and retention (EPR) effect of these NPs. These nanoreactors with deep tissue penetration of NIR-II laser (1060 nm) exhibited concentration-, pH-, and laser power density-dependent PTT outcomes (Figure 9e). The acidic condition of the TME allows for tumor-specific temperature increment with minimal side effects on the neutral pH of healthy adjacent cells. Likewise, the PA signal of the tumor site of animals treated with TCPR NPs appeared 2 h post-injection and increased over time, suggesting a great tumor uptake of the NPs (Figure 9f). Intratumoral ROS levels, immunohistochemistry assay, and in vivo antitumor performance (Figure 9g) revealed that TCPR + NIR groups induced the most severe damage on 4T1 tumor-bearing mice with negligible kidney, liver, and blood toxicities. $CuO_2$ NPs with excellent $H_2O_2$ self-production capacity and TMB with remarkable •OH-activated photothermal efficiency in the NIR-II region proved to be an interesting approach to tumor-specific treatment and imaging with negligible side effects. CDT can be integrated into chemotherapy and PTT approaches on a single platform to further heighten the outcome of $CuO_2$-based cancer therapy and overcome the current challenges. In this respect, $CuO_2$ and DSF were encapsulated in the tips of a microneedle (MN), which consisted of *Panax notoginseng* polysaccharide (PNPS) and PVP in the substrates, resulting in the preparation of

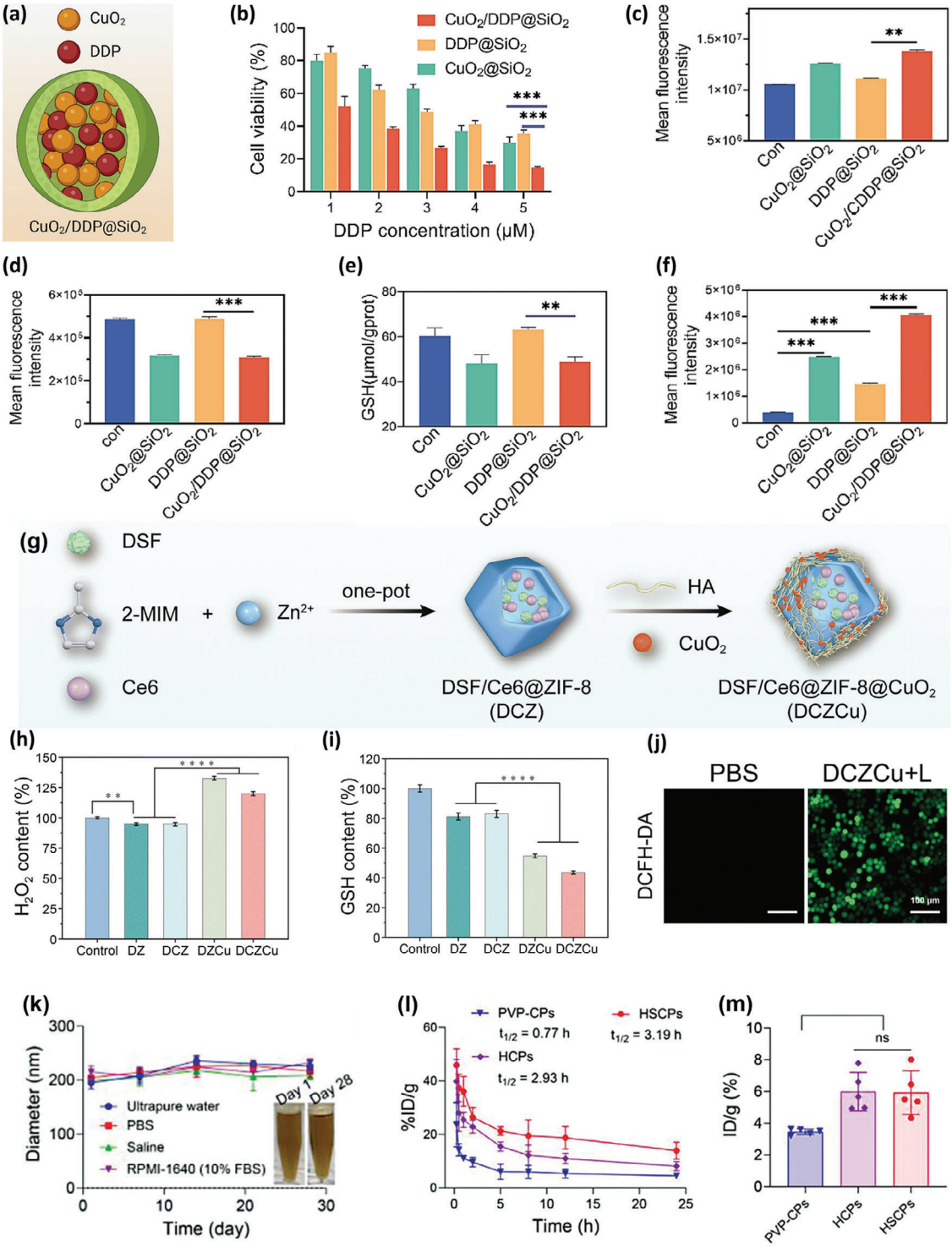


**Figure 8.** a) Schematic illustration of the $CuO_2$/DDP@$SiO_2$ NPs by co-loading of $CuO_2$ and cisplatin inside silica NPs. Created on Biorender.com. b) Cell viability assay of different treatments for 24 h. c) pH values of H22 cells after different treatments. d) $O_2$ levels in hypoxic H22 cells after incubation with various NPs. e) GSH content of H22 cells treated with different NPs. f) ROS generation in DCFH-DA-stain H22 cells treated with different samples. The error bars represent the mean ± SD ($n = 3$). $^{**}p < 0.01$, $^{***}p < 0.001$. Reproduced with permission.[85] Copyright 2024, Elsevier B.V. g) Schematic illustration of the synthesis process of DCZCu NPs. h) Intracellular $H_2O_2$ content and i) GSH content in 4T1 cells treated with different NPs ($n = 3$). j) CLSM images of the DCFH-DA probe in 4T1 cells for the control group and DCZCu NPs treated group under laser irradiation. Reproduced with permission.[87] Copyright 2024, Royal Society of Chemistry. k) Stability of HSCPs using different physiological media ($n = 3$). l) Time-dependent concentrations of Cu element in the blood of 4T1-tumor-bearing mice after intravenous injection ($n = 3$). m) The Cu element content in tumor tissues after 12 h of intravenous injection using ICP-OES ($n = 3$). Reproduced with permission.[83] Copyright 2024, Wiley.

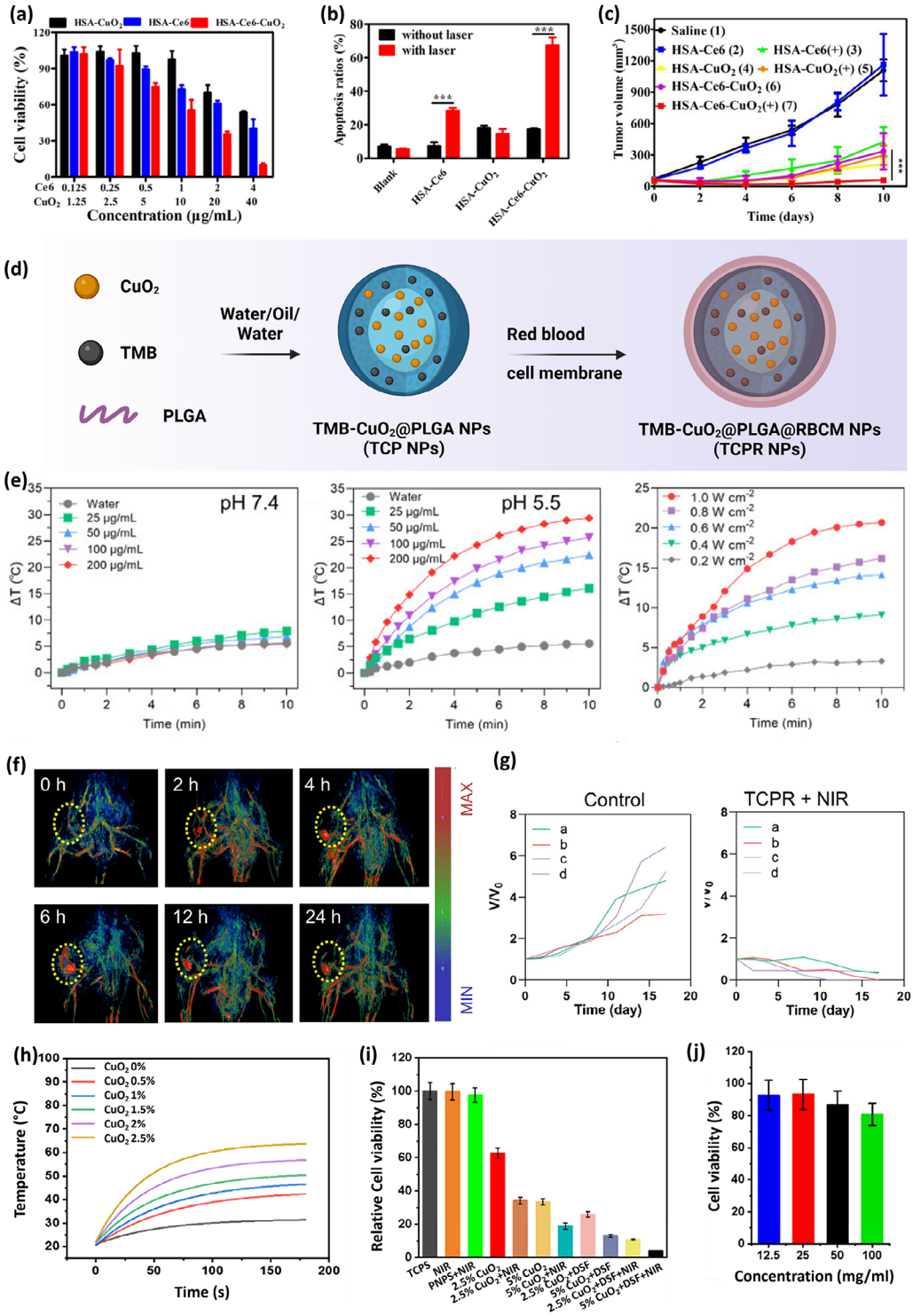


**Figure 9.** a) Cell viability assay of 4T1 cells incubated with different concentrations of HAS-$CuO_2$, HSA-Ce6, and HSA-Ce6-$CuO_2$ using laser irradiation. b) Evaluation of apoptosis induced by different treatment groups utilizing flow cytometric analysis of 4T1 cells. c) The tumor volume rate of the group treated with different therapeutic formulations in 10 days. Data are presented as mean ± SD ($n = 3$). $^{***}p < 0.001$. Reproduced with permission.[81] Copyright 2022, Elsevier B.V. d) Schematic illustration of the synthesis of the TCPR NPs. Created on Biorender.com. e) The quantitative temperature curve of TCPR NPs has different concentrations, pH, and laser power densities. f) Evaluation of the TCPR NPs accumulation was done using copper red acid staining over 24 h of the study. g) Relative tumor volume of the animals after different treatments. Reproduced with permission.[46] Copyright 2024, Elsevier B.V. h) Temperature change curves of different MN systems containing different mass ratios of $CuO_2$ under the 808 nm laser irradiation (1 W $cm^{-2}$) for 3 min. Cell viability of i) B16F10 melanoma cells and j) L929 mouse fibroblast cells after 24 h incubation. Reproduced with permission.[88] Copyright 2023, American Chemical Society.

**Table 4.** Critical paradigms of $ZnO_2$-based biomaterials for various cancer treatments.

| Biomaterial | Size | Dose in vitro (cell viability); in vivo | Cancer type | In vitro cell line | In vivo model | Application | Refs. |
|---|---|---|---|---|---|---|---|
| Mn-$ZnO_2$ NPs | 50 nm | 30 μg $mL^{-1}$ (≈20%); 5 mg $kg^{-1}$ | Glioblastoma | U87MG | U87MG bearing mice | CDT | [6] |
| $ZnO_2$@PEG NPs | 100 nm | 80 μg $mL^{-1}$ (≈40%); 400 μg per mouse | Hepatocellular carcinoma | LM3-HCC | LM3 bearing nude mice | CDT | [98] |
| Manganese-enriched $ZnO_2$ NPs | 80 nm | 20 μg $mL^{-1}$ (≈20%); 23.4 μg per mouse | Breast | 4T1 | 4T1 bearing BALB/c | Immunotherapy | [47] |
| SPS@$ZnO_2$ NPs | 120 nm | 4 μg SPS $mL^{-1}$ (≈2%); 10 mg $kg^{-1}$ | Breast | 4T1 | 4T1 bearing BALB/c | PDT | [99] |
| $ZnO_2$@Au@ZIF-67 NPs | 60 nm | 4 μg $mL^{-1}$ (≈60%); 2.5 mg $kg^{-1}$ | Breast | 4T1 | 4T1 bearing Kunming mice | CDT/ST | [100] |
| $ZnO_2$@Lip-ICG NPs | 205 nm | 207.6 μg $mL^{-1}$ of $ZnO_2$ (≈13%); 5 mg ICG $kg^{-1}$ | Nasopharyngeal carcinoma | CNE-2 | CNE-2 bearing BALB/c nude mice | PDT/PTT | [93] |
| $ZnO_2$@Pt NPs | 120 nm | 200 μg $mL^{-1}$ (≈26%); 100 μg per mouse | Breast | 4T1 | 4T1 bearing BALB/c | CDT/Ion-interference therapy | [94] |
| UCNPs-Hypericin @$mSiO_2$@PEI-siRNA@$ZnO_2$@HA | 61 nm | 2 mg $mL^{-1}$ (17%); 200 μg per mouse | Breast | 4T1 | 4T1 bearing BALB/c | PDT/ Ion-interference therapy/fluorescent imaging | [101] |

Abbreviations: HA: hyaluronic acid; ICG: indocyanine green; $mSiO_2$: mesoporous silica; PEG: polyethylene glycol; PEI: Polyethylenimine; Pt NPs: platinum nanoparticles; siRNA: small interfering ribose nucleic acid; SPS: sinoporphyrin sodium; UCNP: upconversion NPs;‘ ZIF-67: zeolitic imidazolate framework-67.

MN@PNPS@DSF@$CuO_2$ system for CDT/PTT/chemotherapy in melanoma treatment.[88] 10 nm uniformly sized $CuO_2$ NPs succeeded in making a significant temperature change ($\Delta T$) up to 43 °C with 2.5% of mass fraction in the MN system under the 808 nm laser irradiation with a power density of 1 W $cm^{-2}$ for 3 min, representing it as a feasible tool for PTT (Figure 9h). Moreover, 2.5% of the $CuO_2$ NPs in this system under laser irradiation resulted in 10.8% cell viability in B16F10 murine melanoma cells; however, the cell viability of the L929 mouse fibroblasts treated with the same concentration of the NPs was 93.3%, showing excellent tumor killing behavior as well as biocompatibility (Figure 9i,j). Representation of photothermal behavior and chemodynamic therapy from $CuO_2$ NPs beside the chemotherapeutic effect of DSF led to significant tumor inhibition of MN@PNPS@DSF@$CuO_2$ treated animal groups compared to the control group. Collectively, due to the in situ formation of the CuET ($CuO_2$ + DSF), developed transdermal microneedle with satisfactory biocompatibility and excellent combined anti-cancer ability suggested a safe alternative approach for melanoma treatment.

### 3.5.3. Zinc Peroxide ($ZnO_2$)

Compared to other metal ions that have been used in cancer therapy with Fenton/Fenton-like reactions, $ZnO_2$ has the advantage of being more stable at neutral pH, decomposing to $H_2O_2$ and $Zn^{2+}$ at a mildly acidic pH, which is favorable for pH-responsive release in the tumor tissue.[93] In addition, the released $Zn^{2+}$ (like $Ca^{2+}$) ions can mediate ion interference therapy, inhibiting the enzymes in glycolysis, such as hexokinase II and lactate dehydrogenase A, disrupting the redox metabolism and, subsequently, cancer cell death.[94] Thus, $ZnO_2$ NPs offer great potential in ROS-based cancer therapies.

*Synthesis of the $ZnO_2$ NPs*: $ZnO_2$ NPs have the most versatile synthesis methods among other metal peroxides, ranging from hydrothermal synthesis,[95] laser ablation, sol–gel synthesis,[96] and precipitation.[97] In the precipitation method, zinc salts were dissolved in ethanol or methanol. Then, after pH adjustment with NaOH or $NH_4OH$, $H_2O_2$ was added dropwise to successfully synthesize the $ZnO_2$ NPs, which is described in Equation (5).

$$Zn(NO_3)_2 + H_2O_2 + 2NH_4OH \rightarrow ZnO_2 + 2NH_4NO_3 + 2H_2O \quad (5)$$

Moreover, to improve the stability and dispersibility of these NPs, surfactants like PVP and PEG 2000 were utilized.[6,98]

*$ZnO_2$ and Its Role in Cancer Therapy*: Given that $ZnO_2$ can produce $Zn^{2+}$ and $H_2O_2$ in a way that is responsive to the TME pH, several researchers have investigated it as a cancer therapeutic (**Table 4**). For instance, Lin et al. designed a PVP-modified $ZnO_2$ nanostructure as a ROS-generating agent for oxidative stress-mediated cancer cell death.[6] The $ZnO_2$ NPs were doped with paramagnetic manganese for the MRI contrast via a cation-exchange method. The TEM images demonstrated that $ZnO_2$ NPs were stable at pH 7.4 but degraded at pH 5.5 (**Figure 10a**). These NPs displayed excellent cytotoxic ability in glioblastoma cell lines, showing only 20% cell viability at concentrations as low as 30 μg $mL^{-1}$. Further, the in vivo anti-cancer ability of $ZnO_2$ NPs showed significant inhibition of tumor growth (Figure 10b). In contrast, $H_2O_2$ and $ZnCl_2$ treated cells showed negligible tumor growth suppression due to the importance of the controlled release of $Zn^{2+}$ and $H_2O_2$ in the TME. Thus, synergistic oxidative stress-induced tumor cell death was confirmed by $ZnO_2$ NPs due to the inhibition of the electron transfer chain of mitochondria by $Zn^{2+}$ and the exogenous release of $H_2O_2$.

In another study, Tang et al. exploited PEG-modified $ZnO_2$ NPs to apply a rapid burst of zinc ions and $H_2O_2$ inside

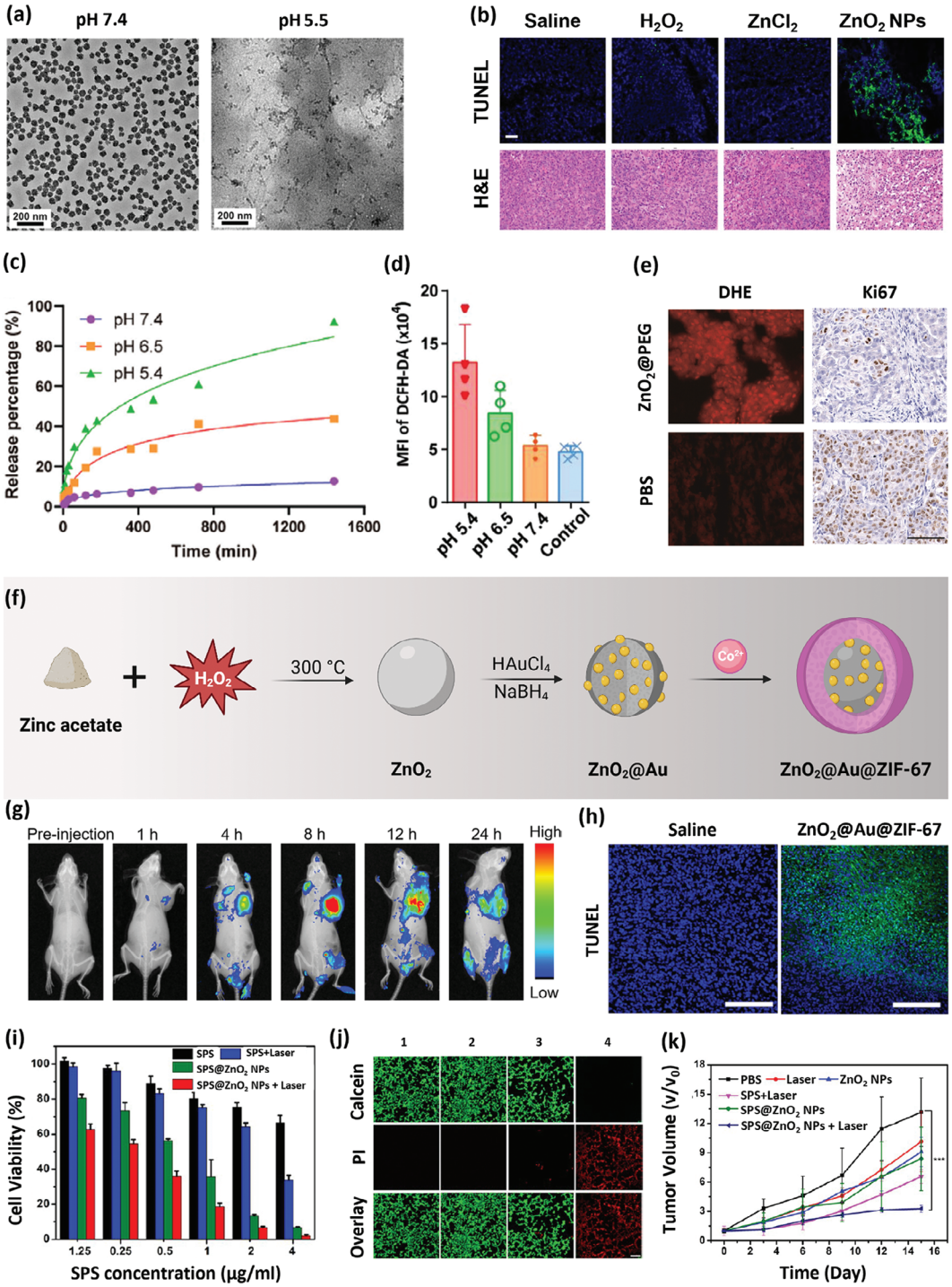


**Figure 10.** a) TEM images of $ZnO_2$ NPs 2 h post-incubation in pH 7.4 and pH 5.5 buffer solutions. b) H&E and TUNEL staining of tumor tissues of different groups. Scale bar, 50 μm. c) Reproduced with permission.[6] Copyright 2019, Ivyspring International Publisher. The release curve of $Zn^{2+}$ ion from $ZnO_2$@PEG NPs (600 μg $mL^{-1}$ Zn in 500 mL solution) at various pH. d) Quantitation of in vitro intracellular ROS generation utilizing DCFH-DA probes via flow cytometry ($n = 4$, mean ± SD). e) DHE staining of HCC sections. And Ki67 positive cells in tumor tissue ($n = 3 \times 10$, mean ± SD), ****$p < 0.0001$, Scale bar = 100 μm. Reproduced with permission.[98] Copyright 2022, Wiley. f) The schematic illustration of the synthesis of $ZnO_2$@Au@ZIF-67 NPs. Created on Biorender.com. g) Real-time fluorescence imaging of 4T1-tumor-bearing mice before and after intravenous injection of Cy7-labeled $ZnO_2$@Au@ZIF-67 NPs. h) Fluorescence images of TUNEL stained (Scale bar: 200 μm) and H&E staining of tumor biopsies treated with $ZnO_2$@Au@ZIF-67 NPs, Scale bar: 400 μm. Reproduced with permission.[100] Copyright 2023, Elsevier B.V. i) Cell viability of 4T1 cells under exposure to various concentrations of SPS and SPS@$ZnO_2$ NPs with and without irradiation. j) Calcein-AM/PI-stained fluorescence images of 4T1 cells treated with different groups: 1) control, 2) laser, 3) SPS@$ZnO_2$ NPs, and 4) SPS@$ZnO_2$ NPs + laser. Scale bar: 20 μm. k) The tumor volume of mice-bearing 4T1 tumors treated with different groups. Reproduced with permission.[99] Copyright 2021, American Chemical Society.

cancer cells and amplify Fenton/Fenton-like reactions with intrinsic Fe to treat orthotopic liver cancer.[98] The $ZnO_2$ NPs showed very high released amounts of $Zn^{2+}$ ions at pH 6.5 and 5.4, which were 44% and 93%, respectively, compared to 13% for the pH 7.4 group (Figure 10c). This result highlights the selectivity of the NPs in the prolonged generation of $Zn^{2+}$ and $H_2O_2$ in healthy liver tissues while the fast degradation of these NPs in an acidic environment. Additionally, in in vivo experiments, tumor regions revealed more ROS production than healthy tissues when treated with the NPs (Figure 10d). Accordingly, the cell proliferation and metastasis index reduced fourfold in the $ZnO_2$@PEG NPs-treated group compared to the control group (Figure 10e). These results indicate that passively accumulated NPs in liver cancer tissues generate $H_2O_2$ and $Zn^{2+}$ for efficient Fenton reaction to produce the highly toxic $^{\bullet}OH$ without any significant side effects to healthy cells. $ZnO_2$ NPs have also been combined with other treatment modalities to improve the therapeutic effects of $ZnO_2$ NPs. Xu et al. developed $ZnO_2$@Au@ZIF-67 NPs based on $^{\bullet}OH$ mediated CDT in combination with glucose-exhausting ST,[100] which consumed glucose at a greater rate than even GOx (Figure 10f). First, the $ZnO_2$ NPs were prepared by underwater Leidenfrost nanochemistry, followed by the reduction of the ultra-small Au NPs on the surface of $ZnO_2$ NPs. Then, the surface was coated with ZIF-67 using an in situ template-assisted method. In vivo biodistribution studies exhibited selective targeting of this nanocatalytic NPs toward the 4T1 cancer model within 12 h (Figure 10g), and tumor sections of $ZnO_2$@Au@ZIF-67 NPs-treated 4T1 bearing mice showed extensive cell death (Figure 10h). This is attributed to the decomposition of the ZIF-67 shell and release of the Fenton-like catalyst $Co^{2+}$ in the TME, followed by exposure of $ZnO_2$@Au, which readily decomposed to generate $O_2$ and $H_2O_2$. Overall, while the glucose consumption caused the starvation of tumor cells, the dual $H_2O_2$ sources promote CDT through reaction with the catalyst $Co^{2+}$, resulting in an enhanced antitumor effect in vivo. In another work, a TME-responsive nanoplatform composed of sinoporphyrin sodium (SPS) photosensitizer-loaded $ZnO_2$ NPs (SPS@$ZnO_2$ NPs) was synthesized for fluorescence-imaging-guided molecular dynamic therapy (MDT)/PDT synergistic cancer therapy.[99] Then, the photosensitizer SPS was loaded onto $ZnO_2$ NPs through the solution-phase reaction. The resulting SPS@$ZnO_2$ NPs were able to quickly degrade into $H_2O_2$ and endogenous $Zn^{2+}$ in an acidic tumor environment and produced toxic $^1O_2$ under 630 nm laser irradiation. The in vitro cytotoxicity test on 4T1 cells showed a much higher cell death rate (>81%) for the SPS@$ZnO_2$ NPs + laser-treated group in comparison to other groups alone (Figure 10i,j). The combination therapy group showed almost complete tumor eradication in 4T1 tumor-bearing mice compared to the other treatments alone (Figure 10k). Taken together, these results prove the efficacy of this multifunctional nanomaterial as a selective cancer theranostic treatment.

In another study, indocyanine green (ICG)-loaded lipid-coated $ZnO_2$ NPs ($ZnO_2$@Lip-ICG) were constructed to self-supply oxygen in TME for efficient oxygen-dependent PDT in the treatment of nasopharyngeal carcinoma.[93] ICG acts as a light-activated photosensitizer and photothermal agent under NIR laser irradiation and was integrated into the liposomes to improve tumor targeting and promote PTT/PDT efficiency. The $ZnO_2$@Lip-ICG NPs were synthesized by the thin film-rehydration method (**Figure 11a**). The temperature elevation profiles showed that the temperature of ICG@Lip and $ZnO_2$@Lip-ICG solutions increased by 22.3 and 26.9 °C, respectively (Figure 11b). The characteristic absorption peak of the $^1O_2$ probe decreased sharply with the $ZnO_2$@Lip-ICG group compared with the free ICG and ICG@Lip groups, likely due to the $O_2$ supply created by the decomposition of $ZnO_2$ (Figure 11c). $^1O_2$ oxidizes the probe resulting in decreasing the absorption peak. In addition, the tumor inhibition rate of the ICG@Lip + laser and $ZnO_2$@Lip-ICG + laser groups were 67.4% and 84.9%, respectively, demonstrating that the oxygen self-supported strategy by $ZnO_2$ effectively enhanced PTT/PDT efficiency for cancer treatment (Figure 11d,e). Combining the CDT properties with immunotherapy, Zhou et al. synthesized TME-responsive manganese-enriched $ZnO_2$ NPs (MONPs) for synergistic antitumor therapy.[47] $ZnO_2$ NPs were enriched with manganese to form MONPs by ion exchange between $Zn^{2+}$ and $Mn^{2+}$. MONPs decomposed in acidic tumor sites and released $H_2O_2$, $Zn^{2+}$, and $Mn^{2+}$. The MONPs produced a higher amount of ROS than $ZnO_2$ due to the conversion of $H_2O_2$ into $^{\bullet}OH$ under the catalysis of $Mn^{2+}$ (Figure 11f). The potent ROS generation could induce ICD and immune response activation in addition to the CDT effect. The MONPs treated cells secreted 2.54-fold higher rates of IFN-$\beta$ in comparison to the $ZnO_2$ NPs treated cells, indicating the stimulatory effect of the $Mn^{2+}$ on interferon gene pathway, which resulted in the secretion of inflammatory cytokines to employ the power of the immune system to diminish immunosuppression of TME (Figure 11h). The results of in vivo antitumor studies showed significantly inhibited tumor growth for MONPs-treated groups, which was further enhanced by adding an anti-PD-1 antibody (Figure 11i,j), confirming the promising therapeutic strategy of CDT-assisted immunotherapy for tumor treatment.

#### 3.5.4. Magnesium Peroxide ($MgO_2$)

Among different metal peroxides, $MgO_2$ possesses characteristics such as high stability, biosafety, and higher theoretical active oxygen contents (28.6 wt%) than $CaO_2$ (22.2 wt%) and $ZnO_2$ (16.5 wt%), suggesting stronger oxidation capacity,[102] which makes it an attractive candidate for generating $H_2O_2$ in cancer therapy approaches. However, the size and purity of $MgO_2$ affect its performance.

*Synthesis of the $MgO_2$ NPs*: $MgO_2$ NPs were synthesized through a reverse microemulsion-like method by dissolving $MgCl_2$ in an aqueous solution, followed by the addition of cyclohexane and polyoxyethylene (5) nonylphenylether as a nonionic surfactant.[26,103] Then, after the addition of ammonium hydroxide and the formation of $Mg(OH)_2$, the $H_2O_2$ was added dropwise to form the $MgO_2$ NPs, which is represented in Equation (6).

$$MgCl_2 + H_2O_2 + 2NH_4OH \rightarrow MgO_2 + 2NH_4Cl + 2H_2O \quad (6)$$

Moreover, some of the studies found that these metal peroxides could be achieved by adding $H_2O_2$ to MgO nanoparticles.[104]

*$MgO_2$ and Its Role in Cancer Therapy*: As summarized in **Table 5**, various studies have been conducted on the effectiveness of $MgO_2$ NPs across different cancer models, representing

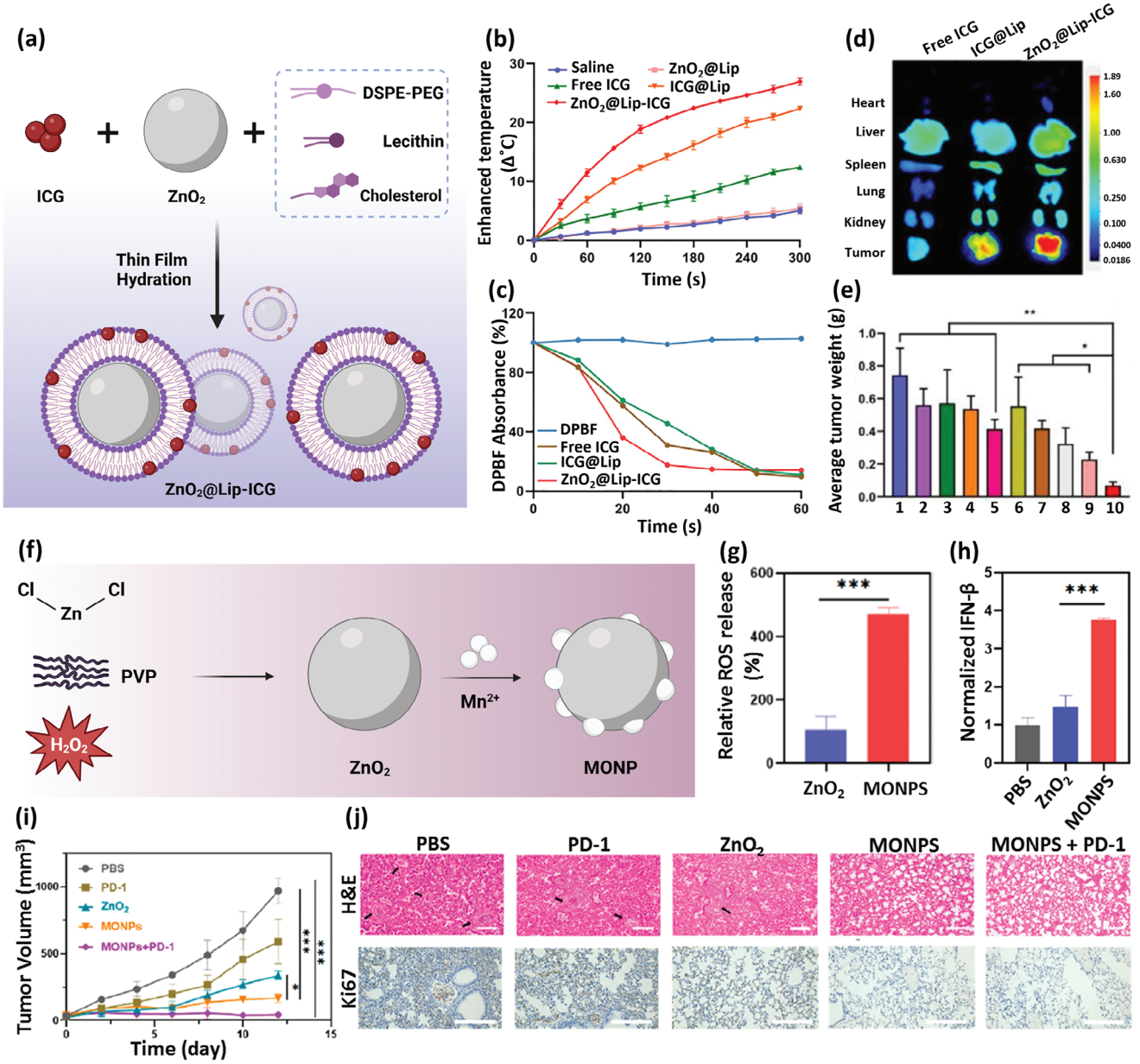


**Figure 11.** a) The schematic illustration of synthesis procedure of $ZnO_2$@Lip-ICG NPs. Created on Biorender.com. b) The thermal plots of different solutions under 808 nm laser irradiation (1 W $cm^{-2}$, 5 min) ($n = 5$). c) The $^1O_2$ generation of different groups irradiated by 808 nm laser for 5 min. d) Fluorescence images of main organs and tumor sections of CNE-2 tumor-bearing mice 24 h after injection. e) Tumor weight of CNE-2 tumor-bearing mice treated with different groups; 1: Saline, 2: $ZnO_2$@Lip, 3: Free ICG, 4: ICG@Lip, 5: $ZnO_2$@Lip-ICG, 6: Saline+Laser, 7: $ZnO_2$@Lip+Laser, 8: Free ICG+Laser, 9: ICG@Lip+Laser, 10:$ZnO_2$@Lip-ICG+Laser, ($n = 5$), $^*p < 0.05$, $^{**}p < 0.01$. Reproduced with permission.[93] Copyright 2022, Elsevier B.V. f) Schematic illustration of the synthesis procedure of the MONPs. Created on Biorender.com. g) Relative ROS release from different NPs in pH 5.5. h) The secretion amount of IFN-$\beta$ incubated with $ZnO_2$ NPs and MONPs. All data were expressed as mean ± SD ($n = 3$). $^{***}p < 0.001$. i) The tumor volume of 4T1-bearing mice after different treatments. j) H&E and Ki67 staining of lungs with different treatments. Scale bar: 500 µm. Data were expressed as mean ± SD ($n = 5$). $^*p < 0.05$, $^{***}p < 0.00$. Reproduced with permission.[47] Copyright 2023, American Chemical Society.

their potential in both monotherapy and multitherapy of cancer disease. For instance, Wu et al. synthesized spherical granular $MgO_2$ NPs with a diameter of around 40 nm, which showed concentration-dependent •OH generation capacity in vitro.[104a]

In another attempt, transferrin-modified $MgO_2$ nanosheets (TMNSs) were synthesized to react with $H^+$ in the TME, producing sufficient $H_2O_2$ required in Fenton reaction ($MgO_2 + 2H^+ \rightarrow Mg^{2+} + H_2O_2$).[26] Therefore, $H_2O_2$ disrupts the structure of the transferrin on the surface, leading to the release of trapped $Fe^{3+}$ and, subsequently, the generation of the highly toxic •OH in the Fenton reaction. Higher $H_2O_2$ generation and stronger •OH signals were observed in acidic environments compared to the neutral pH, confirming the excellent biodegradability of the TMNSs in acidic pH. The anti-tumor

**Table 5.** Critical paradigms of $MgO_2$-based biomaterials for various cancer treatments.

| Biomaterial | Size | Dose in vitro (cell viability); in vivo | Cancer type | In vitro cell line | In vivo model | Application | Refs. |
|---|---|---|---|---|---|---|---|
| Transferrin-modified $MgO_2$ nanosheets | 100–200 nm | 25 μg $mL^{-1}$ (≈60%); 100 mg $kg^{-1}$ | Breast and lung | 4T1; Lewis | 4T1 and Lewis bearing BALB/c | CDT | [26] |
| Hf-MOF-$MgO_2$/DNA NPs | 200 nm | 40 μg $mL^{-1}$ (≈15%); 100 μg per mouse | Lung and breast | A549; 4T1 | 4T1 bearing BALB/c | PDT | [104b] |
| $MgO_2$/PLGA scaffolds | 50–95 nm | 100 μg $mL^{-1}$; 1 scaffold with 20 wt% $MgO_2$ | Osteosarcoma | 143B | 143B bearing BALB/c | CDT/antibacterial/ osteogenic | [105] |
| PCL/nHA/$MgO_2$/PDA-integrated scaffold | – | – | Osteosarcoma | F143B | F143B bearing BALB/c | CDT/PTT/Bone repair | [106] |
| $MgO_2$@$SnFe_2O_4$@PEG nanoplatform | 50–300 nm | —; 5 mg $kg^{-1}$ | Cervical carcinoma | HeLa | HeLa bearing BALB/c nude mice | CDT/PTT/PDT | [48] |
| Ce6, $MgO_2$-$Fe_2O_3$/CNx-Ce6 nanoplatform | – | 80 μg $mL^{-1}$ (≈30%); 200 μg per mouse | Breast | 4T1 | 4T1 bearing BALB/c | CDT/PDT | [103] |

Abbreviations: Ce6: Chorin-e6; PCL: polycaprolactone; PDA: polydopamine; PEG: polyethylene glycol; PLGA: poly lactic-co-glycolic acid; nHA: nanohydroxyapatite.

activity of TMNSs was conducted on 4T1 tumor-bearing mice via intravenous and intratumoral (i.t.) injection. H&E stained tumor sections showed significant necrosis and apoptosis in intravenously injected animals, while it was even more severe in the i.t. injected group. Therefore, TMNSs displayed excellent cancer treatment outcomes, owing to delivering high concentrations of $H_2O_2$ and $Fe^{3+}$ to cancer cells in a pH-dependent manner. With the same method of $MgO_2$ NPs synthesis, Zhang et al. proposed a nanoplatform based on $SnFe_2O_4$ decorated $MgO_2$ (MSnFeP) for simultaneous $H_2O_2$ self-supply, GSH depletion, and phototherapy for CDT, PTT, and PDT.[48] $SnFe_2O_4$, a bimetallic oxide, simultaneously plays a role as a GSH-depleting agent, chemodynamic, and photoactive agent. The MSnFeP+NIR light group revealed the highest •OH generation in HeLa cancer cells. The in vivo antitumor efficacy on the HeLa tumor-bearing mice model exhibited the restrained tumors to a certain extent in the $SnFe_2O_4$+NIR treated group, showing the collaborative tumor destruction effect of PTT and PDT. However, distinct tumor suppression occurred in the groups treated with MSnFeP+NIR, suggesting the importance of using $MgO_2$ NPs as an $H_2O_2$ donor for intensified cancer therapy outcomes with CDT, PTT, and PDT. Collectively, these results are attributed to three reasons. First, $Fe^{2+}$/$Sn^{2+}$ converts the $MgO_2$-generated $H_2O_2$ to •OH through a Fenton/Fenton-like reaction. Secondly, these metal ions consume the upregulated GSH via redox reaction, leading to increased efficiency of ROS. Thirdly, NIR light triggers PDT to produce ROS and hyperthermia-enhanced CDT. Furthermore, with the aim of using synergistic treatment modalities to achieve better outcomes from cancer treatment, a 3D-printed polycaprolactone (PCL)/nanohydroxyapatite (nHA)/$MgO_2$/PDA scaffold was designed as a dual functional therapeutic implant with excellent PTT behavior and ROS generation for tumor elimination and subsequent bone defect repair of osteosarcoma.[106] PCL and nHA with local osteogenesis stimulation and great mechanical strength and PDA with magnificent PTT ability were incorporated inside the scaffold. This study was designed to prepare different scaffolds, including bare scaffold (PH), three different concentrations of the $MgO_2$ of 5% (P5 M), 10% (P10 M), and 15% (P15 M), and one concentration of the MgO (10%, PO) incorporated in the scaffold. In vitro osteogenic performance of the bone mesenchymal stem cells (BMSCs) displayed hampered cell proliferation in hypoxic conditions with the P15 M treated group due to the apoptotic effect of the high concentration of the $Mg^{2+}$ and $H_2O_2$ on BMSCs (**Figure 12a**). Also, PH, PO, and P5 M showed the same behavior in suppressing cell proliferation, suggesting the importance of reversing hypoxia in the proliferation of the BMSCs. Whereas the P10 M scaffolds exhibited sufficient $O_2$-producing ability with low cytotoxicity in hypoxic conditions to proceed. Also, the downregulation of HIF-1$\alpha$ and upregulation of the osteogenic-related genes was demonstrated with the P10 M treated group in BMSCs cells, resulting in osteogenic repair (Figure 12b). The results of in vivo studies were consistent with in vitro experiments, showing the significantly enhanced amount of bone mineral density in the P10 M treated group compared to other groups, signifying better osteogenic performance by reversing the hypoxia (Figure 12c). The anti-tumor activity on F143B osteosarcoma cells under hypoxic conditions displayed a higher apoptotic rate in the P10 M treated group in comparison to the other groups (Figure 12d). After obtaining superior in vitro anti-tumor performance, the P10 M + NIR group in in vivo studies had efficient tumor suppression by exhibiting decreased tumor volume, loose tissue structure, missing nuclei in most tumor cells, and a high apoptotic rate compared to the other groups (Figure 12e,f). Hence, this bifunctional scaffold provides a unique and efficient approach for tumor-based bone defect repair and antitumor performance for osteosarcoma treatment. In another combination cancer treatment study, $Fe_2O_3$/CNx nanoreactor with dual enzyme simulated activity modified by $MgO_2$ and photosensitizer Ce6 to synthesize $MgO_2$-$Fe_2O_3$/CNx-Ce6 (MFCC) platform for combined CDT/PDT (Figure 12g).[103] CNx sheet was used as a carrier and reducing agent to convert $Fe_2O_3$ to $Fe^{2+}$, in which the generated $Fe^{2+}$ can react with released $H_2O_2$ from $MgO_2$ to produce •OH and $Fe^{3+}$. Next, the generated $Fe^{3+}$ can deactivate GSH and become converted to $Fe^{2+}$, completing the cycle and reaching higher outcomes of ROS-based cancer

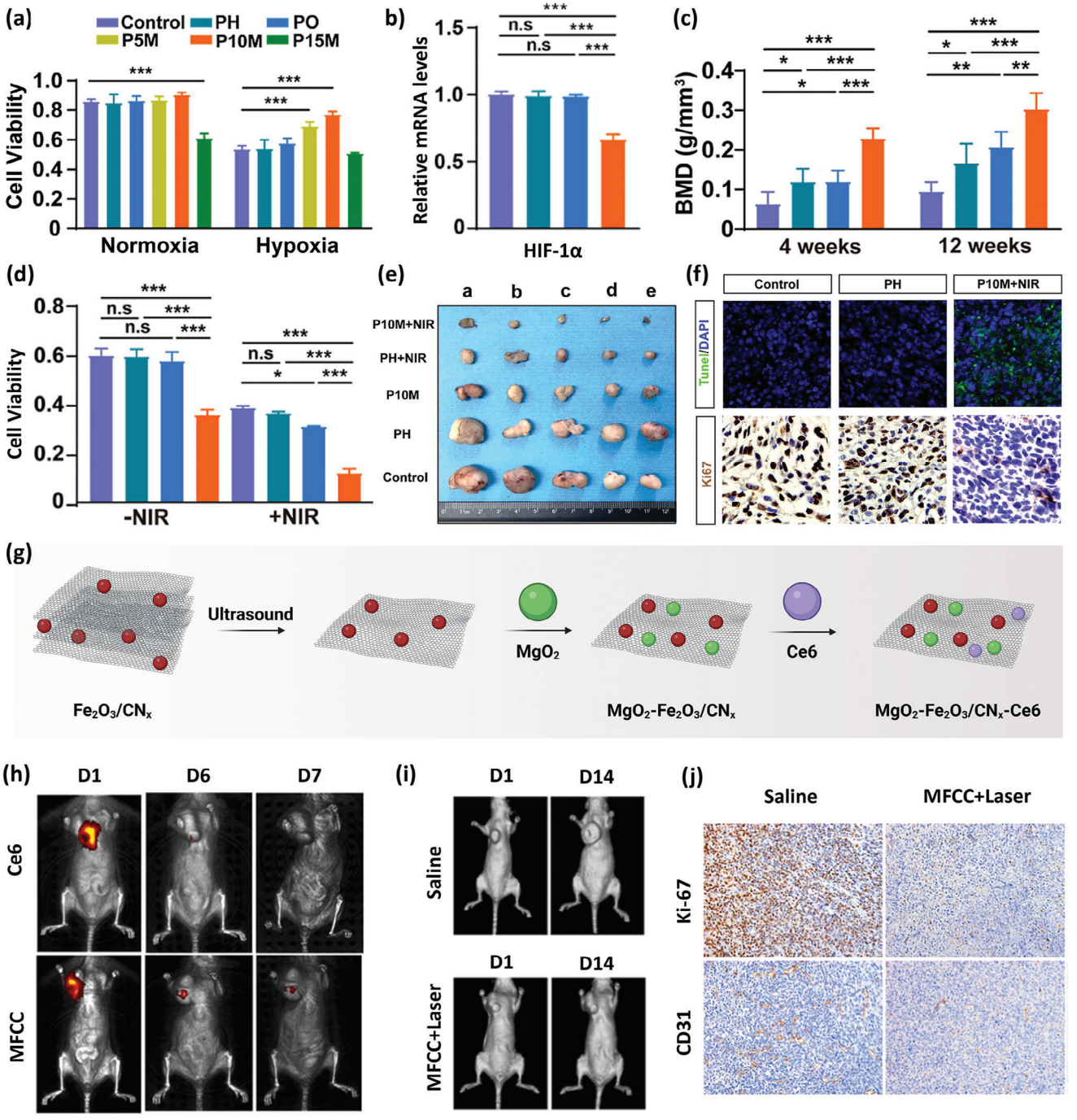


**Figure 12.** a) Cell viability of BMSCs treated with different scaffolds in normoxic and hypoxic conditions. b) Quantitative RT-PCR of HIF-1$\alpha$ mRNA expression of BMSCs treated with different groups after osteogenic induction. c) Bone mineral density of different treated groups in 1 and 3 months after surgery. d) Cell viability analysis of F143B osteosarcoma cells under a hypoxic environment treated with control, PH, PO, and P10 M scaffolds. Data are presented as mean ± SEM ($n = 6$). *$p < 0.05$, **$p < 0.01$, and ***$p < 0.001$; n.s., no significance. e) Representative tumor images were excised from the sacrificed mice. f) Histological TUNEL and Ki67 analyses of tumor sections in control, PH, and P10 M treated groups. Reproduced with permission.[106] Copyright 2024, American Chemical Society. g) Schematic illustration of the MFCC synthetic process. Created on Biorender.com. h) The in vivo fluorescence images of the 4T1 bearing mice treated with Ce6 and MFCC on different days. i) CT scans of mice representing the size of tumor tissue on the different days. j) Ki67 and CD31 staining on the tumor tissues of saline and MFCC + laser-treated group. Scale bar: 50 µm. Reproduced with permission.[103] Copyright 2024, Elsevier B.V.

therapy. MFCC platform displayed multiple functions, including excellent behavior in $H_2O_2$ self-production, $Fe^{2+}$ release, $O_2$ generation, GSH depletion, ROS generation, and hypoxia relief in extracellular and intracellular studies. Ce6 not only can induce PDT in the system, but also can act as a fluorescent agent in this platform, tracking the accumulation of treatment at the tumor site and demonstrating the diagnostic applications. The fluorescence of the MFCC treatment group showed an extended fluorescence signal compared to the free Ce6 group, signifying the accumulation of the platform for a prolonged time in tumor tissues due to the EPR effect, leading to an enhanced antitumor effect (Figure 12h). Considering the valuable results from in vitro studies, an in vivo anti-tumor experiment on 4T1-bearing mice after 14 days showed the inhibited increase in tumor volume in the MFCC + Laser group, indicating a synergistic role of CDT and PDT in killing 4T1 cells under laser irradiation (Figure 12i). Also, immunohistochemical staining observing the expression of CD31 and Ki-67 displayed the inhibited expression of angiogenic factors, thereby inhibiting tumor neovascularization and growth in the MFCC + Laser treated group (Figure 12j). Hence, this study showed the potential of the CDT/PDT synergistic therapy in representing anti-tumor performance with a single multi-function platform.

## 4. Conclusions and Future Perspectives

The field of oncological research is in desperate need of more specific and effective anti-cancer therapies. In recent years, increasing the concentration of $H_2O_2$ has arisen as a promising strategy to intensify the outcome of the different treatment modalities. Several approaches include the delivery of exogenous $H_2O_2$, preventing $H_2O_2$ consumption, producing $H_2O_2$ from glucose, water, and oxygen, and using metal peroxides to deliver the $H_2O_2$ to TME and disrupt the redox homeostasis in tumor cells. Metal peroxides, in particular, exhibit great potential for anti-cancer therapy, owing to their specificity to the abnormal TME (low pH and high GSH concentration) and their ability to normalize the hypoxia. Among the representative metal peroxides, $CaO_2$ has been the most extensively explored due to its established capacity to produce $H_2O_2$ in a controlled manner and its observed biocompatibility. However, other metal peroxides, such as $CuO_2$, $ZnO_2$, and $MgO_2$, are increasingly stepping up as alternatives with advantages such as inducing Fenton-like reactions, versatility in synthesis methods, and superior biocompatibility, respectively. Especially when used in combination with PDT, PTT, chemotherapy, or immunotherapy, metal peroxide-based treatments show excellent anti-cancer efficacy and minimal damage to adjacent healthy tissues.

Despite the promising opportunities of $H_2O_2$-generating platforms for anticancer purposes, their clinical translation faces many challenges. Achieving clinical success requires fundamental features, including reproducibility, large-scale synthesis, biocompatibility, and satisfactory efficacy in clinical trials. Furthermore, long-term stability and accurate targeted delivery ensure a satisfactory anti-tumor effect while avoiding off-target effects. In this context, rational design and the usage of optimal nanoformulations are required to enhance NPs' exposure to the tumor site. Uniformity in size and shape as well as NPs' stability in biological systems are another challenges that must be addressed. Throughout many studies, the size observed in TEM images did not correspond with hydrodynamic size measurements. This inconsistency in presenting the characterization data suggests more accurate techniques for measuring the uniformity of NPs. Additionally, establishing standardized protocols for measuring in vivo $H_2O_2$ concentration is essential for comparing and optimizing the efficiency of different nanoplatforms. Furthermore, treatments that exploit the differences between healthy and cancer tissues are limited primarily by our understanding of these environments. Careful attention should be paid to the molecular mechanisms underlying the altered redox homeostasis in cancer tissues and how these may differ for various cancer types. In doing so, improved cancer treatments can be created, using the healthy human body as a blueprint.

Finally, ROS-based cancer treatments provide an optimistic outlook on the future of cancer treatment. Their clinical application may provide the future of cancer therapies, where potency and specificity are combined for a more effective and less invasive treatment. However, fundamental research is still needed to address clinical, regulatory, and commercial concerns.

## Acknowledgements

Prof. H.A.S. acknowledges financial support from the UMCG Research Funds. Dr. M.-A.S. acknowledges Incentive fund from the University of Groningen and financial support from the UMCG Research Funds.

## Conflict of Interest

The authors declare no conflict of interest.

## Keywords

cancer therapy, chemodynamic therapy, metal peroxide nanoparticles, photodynamic therapy, ROS

Received: December 28, 2024
Revised: February 4, 2025
Published online:

[1] E. Panieri, M. M. Santoro, *Cell Death Dis.* **2016**, *7*, e2253.
[2] a) Y. Zhang, J. Zhang, Q. Jia, J. Ge, P. Wang, *Mater. Chem. Front.* **2021**, *5*, 4474; b) C. He, X. Zhang, G. Xiang, *Biomater. Sci.* **2020**, *8*, 5574.
[3] T. Ali, D. Li, T. N. F. Ponnamperumage, A. K. Peterson, J. Pandey, K. Fatima, J. Brzezinski, J. A. R. Jakusz, H. Gao, G. E. Koelsch, *Cancers* **2024**, *16*, 2171.
[4] P. Yu, X. Li, G. Cheng, X. Zhang, D. Wu, J. Chang, S. Wang, *Chin. Chem. Lett.* **2021**, *32*, 2127.
[5] Y. Tang, Y. Li, B. Li, W. Song, G. Qi, J. Tian, W. Huang, Q. Fan, B. Liu, *Nat. Commun.* **2024**, *15*, 2530.
[6] L.-S. Lin, J.-F. Wang, J. Song, Y. Liu, G. Zhu, Y. Dai, Z. Shen, R. Tian, J. Song, Z. Wang, *Theranostics* **2019**, *9*, 7200.
[7] H. Sies, D. P. Jones, *Nat. Rev. Mol. Cell Biol.* **2020**, *21*, 363.
[8] Q. Zhang, Q. Luo, Z. Liu, M. Sun, X. Dong, *Chem. Eng. J.* **2023**, *457*, 141225.
[9] H. Chen, Z. Gu, H. An, C. Chen, J. Chen, R. Cui, S. Chen, W. Chen, X. Chen, X. Chen, *Sci. China: Chem.* **2018**, *61*, 1503.

 

[10] A. Miar, D. Hevia, H. Muñoz-Cimadevilla, A. Astudillo, J. Velasco, R. M. Sainz, J. C. Mayo, *Free Radicals Biol. Med.* **2015**, *85*, 45.
[11] C. Nicco, A. Laurent, C. Chereau, B. Weill, F. Batteux, *Biomed. Pharmacother.* **2005**, *59*, 169.
[12] A.-G. Niculescu, A. M. Grumezescu, *Appl. Sci.* **2021**, *11*, 3626.
[13] J. Yang, D. Dai, X. Zhang, L. Teng, L. Ma, Y.-W. Yang, *Theranostics* **2023**, *13*, 295.
[14] C. Zhang, W. Bu, D. Ni, S. Zhang, Q. Li, Z. Yao, J. Zhang, H. Yao, Z. Wang, J. Shi, *Angew. Chem., Int. Ed.* **2016**, *55*, 2101.
[15] a) H. Han, J. Li, H. A. Santos, *Biomed. Technol.* **2023**, *3*, 40; b) J. Yang, W. Xiong, L. Huang, Z. Li, Q. Fan, F. Hu, X. Duan, J. Fan, B. Li, J. Feng, Y. Xu, X. Chen, Z. Shen, *J. Nanobiotechnol.* **2024**, *22*, 204.
[16] a) T. He, Q. Tang, Q. Ren, Y. Liu, G. He, Y. Pan, Z. Wang, P. Huang, J. Lin, *ACS Nano* **2024**, *18*, 5434; b) S. Wang, Y. Pang, S. Hu, J. Lv, Y. Lin, M. Li, *Chem. Eng. J.* **2023**, *451*, 138864.
[17] a) Z. Du, X. Wang, X. Zhang, Z. Gu, X. Fu, S. Gan, T. Fu, S. Xie, W. Tan, *Angew. Chem., Int. Ed.* **2023**, *62*, 202302525; b) W. Chen, F. Hu, Q. Gao, C. Zheng, Q. Bai, J. Liu, N. Sun, W. Zhang, Y. Zhang, K. Dong, T. Lu, *J. Nanobiotechnol.* **2024**, *22*, 98.
[18] a) T. Zhang, Q. Zheng, J. Huang, X. Li, *Adv. Funct. Mater.* **2024**, *34*, 2311029; b) G. Zeng, J. Mao, H. Xing, Z. Xu, Z. Cao, Y. Kang, G. Liu, P. Xue, *Adv. Sci.* **2024**, *11*, 2406683.
[19] Q. T. Hoang, D. Y. Kim, H. S. Park, W. Jang, T. G. Nguyen Cao, J. H. Kang, Y. T. Ko, S. J. Mun, S. H. Bhang, M. S. Shim, *Adv. Funct. Mater.* **2024**, 2306078.
[20] J. Yu, F. Zhu, Y. Yang, P. Zhang, Y. Zheng, H. Chen, Y. Gao, *Colloids Surf., B* **2023**, *232*, 113606.
[21] a) B. Qi, W. Wu, Z. Wang, G. Liu, Z. Li, Z. Xiao, *J. Mater. Chem. C* **2024**, *12*, 10135; b) L. Li, Z. Xing, T. Liao, J. Wang, Z. Xu, Y. Kuang, C. Li, *Mater. Today Chem.* **2024**, *39*, 102171.
[22] E. Kirbas Cilingir, O. Besbinar, L. Giro, M. Bartoli, J. L. Hueso, K. J. Mintz, Y. Aydogan, J. M. Garber, M. Turktas, O. Ekim, A. Ceylan, M. A. Unal, M. Ensoy, F. Arı, O. Ozgenç Çinar, B. I. Ozturk, C. Gokce, D. Cansaran-Duman, M. Braun, J. Wachtveitl, J. Santamaria, L. G. Delogu, A. Tagliaferro, A. Yilmazer, R. M. Leblanc, *Small* **2024**, *20*, 2309283.
[23] Y. Xu, J. Bian, X. Liu, Z. Qian, M. Sun, C. Zhang, R. Pan, Q. Li, C. Sun, B. Lin, K. Peng, N. Lu, X. Yao, W. Fan, *Acta Biomater.* **2023**, *172*, 441.
[24] a) G. Su, H. Xu, F. Zhou, X. Gong, S. Tan, Y. He, *ACS Appl. Mater. Interfaces* **2023**, *15*, 59175; b) Z. Li, C. Wang, C. Dai, R. Hu, L. Ding, W. Feng, H. Huang, Y. Wang, J. Bai, Y. Chen, *Biomaterials* **2022**, *287*, 121668.
[25] a) Y. Gao, Z. Ouyang, S. Shen, H. Yu, B. Jia, H. Wang, M. Shen, X. Shi, *ACS Nano* **2023**, *17*, 23889; b) H. Huang, H. Guo, J. Liu, C. Ni, L. Xia, X. Cao, J. Xia, X. Shi, R. Guo, *Acta Biomater.* **2024**, *183*, 252.
[26] Z. m. Tang, Y. y. Liu, D. l. Ni, J. j. Zhou, M. Zhang, P. r. Zhao, B. Lv, H. Wang, D. y. Jin, W. b. Bu, *Adv. Mater.* **2020**, *32*, 1904011.
[27] C. Liu, Y. Cao, Y. Cheng, D. Wang, T. Xu, L. Su, X. Zhang, H. Dong, *Nat. Commun.* **2020**, *11*, 1735.
[28] K. Wu, A. E. El Zowalaty, V. I. Sayin, T. Papagiannakopoulos, *Nat. Cancer* **2024**, *5*, 384.
[29] P. D. Ray, B. W. Huang, Y. Tsuji, *Cell Signal* **2012**, *24*, 981.
[30] J. Xin, C. Deng, O. Aras, M. Zhou, C. Wu, F. An, *J. Nanobiotechnol.* **2021**, *19*, 192.
[31] R. R. Mallepally, C. C. Parrish, M. A. M. M. Hugh, K. R. Ward, *Int. J. Pharm.* **2014**, *475*, 130.
[32] X. Song, J. Xu, C. Liang, Y. Chao, Q. Jin, C. Wang, M. Chen, Z. Liu, *Nano Lett.* **2018**, *18*, 6360.
[33] C. Glorieux, P. B. Calderon, *Redox Biol.* **2024**, *77*, 103404.
[34] G. Li, S. Yuan, D. Deng, T. Ou, Y. Li, R. Sun, Q. Lei, X. Wang, W. Shen, Y. Cheng, Z. Liu, S. Wu, *Adv. Funct. Mater.* **2019**, *29*, 1901932.
[35] N. Aykin-Burns, I. M. Ahmad, Y. Zhu, L. W. Oberley, D. R. Spitz, *Biochem. J.* **2009**, *418*, 29.
[36] C. Liu, J. Xing, O. U. Akakuru, L. Luo, S. Sun, R. Zou, Z. Yu, Q. Fang, A. Wu, *Nano Lett.* **2019**, *19*, 5674.
[37] J. Mu, L. He, W. Fan, W. Tang, Z. Wang, C. Jiang, D. Zhang, Y. Liu, H. Deng, J. Zou, *Small* **2020**, *16*, 2004016.
[38] L. He, Q. Ni, J. Mu, W. Fan, L. Liu, Z. Wang, L. Li, W. Tang, Y. Liu, Y. Cheng, *J. Am. Chem. Soc.* **2020**, *142*, 6822.
[39] X. Wang, B. Sun, Q. Dai, L. Zhu, Z. Gu, L. Dai, *Adv. Mater.* **2024**, *36*, 2408560.
[40] a) J. Ma, C. Peng, X. Peng, S. Liang, Z. Zhou, K. Wu, R. Chen, S. Liu, Y. Shen, H. Ma, Y. Zhang, *J. Am. Chem. Soc.* **2024**, *146*, 21147; b) N. Lagopati, K. Evangelou, P. Falaras, E.-P. C. Tsilibary, P. V. S. Vasileiou, S. Havaki, A. Angelopoulou, E. A. Pavlatou, V. G. Gorgoulis, *Pharmacol. Ther.* **2021**, *222*, 107795.
[41] L. Khoshtabiat, A. Meshkini, M. M. Matin, *Cancer Nanotechnol.* **2023**, *14*, 40.
[42] W. P. Li, C. H. Su, Y. C. Chang, Y. J. Lin, C. S. Yeh, *ACS Nano* **2016**, *10*, 2017.
[43] K. Yang, G. Yu, Z. Yang, L. Yue, X. Zhang, C. Sun, J. Wei, L. Rao, X. Chen, R. Wang, *Angew. Chem., Int. Ed.* **2021**, *60*, 17570.
[44] P. Gao, R. Wei, Y. Chen, X. Li, W. Pan, N. Li, B. Tang, *Biomaterials* **2023**, *297*, 122109.
[45] Y. Hu, X. Wang, P. Zhao, H. Wang, W. Gu, L. Ye, *Biomater. Sci.* **2020**, *8*, 2931.
[46] N. Yang, H. Li, C. Cao, L. Zhao, X. Song, W. Wang, W. Xu, Y. Zhang, P. Chen, X. Dong, *Fundam. Res.* **2024**, *4*, 178.
[47] M. Zhou, S. Liang, D. Liu, K. Ma, K. Yun, J. Yao, Y. Peng, L. Hai, Q. Zhang, Z. Wang, *Nano Lett.* **2023**, *23*, 10350.
[48] H. Zhang, R. Han, P. Song, X. Wei, Y. Hou, J. Yu, K. Tang, *J. Colloid Interface Sci.* **2023**, *629*, 103.
[49] V. L. Prasanna, D. Harikaran, D. Avisar, V. R., *RSC Adv.* **2023**, *13*, 3416.
[50] a) J. Chen, H. Ma, H. Luo, H. Peng, Q. Yan, S. Pu, *J. Hazard. Mater.* **2024**, *464*, 132902; b) C. He, S. Zhang, X. Liu, J. Wang, Y. Huang, A. Zhang, X. Zhang, *Nanotechnology* **2023**, *34*, 482002.
[51] a) A. Rastinfard, M. H. Nazarpak, F. Moztarzadeh, *RSC Adv.* **2018**, *8*, 91; b) H. Mosmeri, E. Alaie, M. Shavandi, S. M. M. Dastgheib, S. Tasharrofi, *Environ. Monit. Assess.* **2017**, *189*, 452; c) X. Li, Y. Du, H. Wang, H. Ma, D. Wu, X. Ren, Q. Wei, J.-J. Xu, *Anal. Chem.* **2020**, *92*, 12693; d) C. Ji, Z. Lu, Y. Xu, B. Shen, S. Yu, D. Shi, *J. Biomed. Mater. Res., Part B* **2018**, *106*, 2544.
[52] a) S. Shen, M. Mamat, S. Zhang, J. Cao, Z. D. Hood, L. Figueroa-Cosme, Y. Xia, *Small* **2019**, *15*, 1902118; b) Y.-C. Chen, Y.-J. Liu, C.-L. Lee, K.-Y. Pham, D. Manoharan, S. Thangudu, C.-H. Su, C.-S. Yeh, *Adv. Healthcare Mater.* **2022**, *11*, 2201613.
[53] a) J. S. Park, Y. J. Song, Y. G. Lim, K. Park, *Materials (Basel, Switzerland)* **2020**, *13*, 3864; b) F. Li, T. S. Y. Choong, L. C. Abdullah, S. N. A. Md. Jamil, N. N. Amerhaider Nuar, *Polymers* **2023**, *15*, 775.
[54] W. Huang, L. Zhang, Q. Yang, Z. Wang, *Chin. J. Chem.* **2014**, *32*, 909.
[55] M. Wiśniewska, I. Ostolska, K. Szewczuk-Karpisz, S. Chibowski, K. Terpiłowski, V. M. Gun'ko, V. I. Zarko, *J. Nanopart. Res.* **2015**, *17*, 12.
[56] H. Yu, J. Sun, K. She, M. Lv, Y. Zhang, Y. Xiao, Y. Liu, C. Han, X. Xu, S. Yang, G. Wang, G. Zang, *Regener. Biomater.* **2023**, *10*, rbad071.
[57] M. Paúrová, O. Taboubi, I. Šeděnková, J. Hromádková, P. Matouš, V. Herynek, L. Sefc, M. Babič, *Eur. Polym. J.* **2021**, *157*, 110634.
[58] N. N. Amerhaider Nuar, S. N. A. Md. Jamil, T. S. Y. Choong, I. D. Mat Azmi, N. A. Abdul Romli, L. C. Abdullah, P.-C. Chiang, F. Li, *Polymers* **2023**, *15*, 1327.
[59] S. Bai, H. Chen, S. Fu, C. Liu, X. Gao, S. Li, Y. Chen, Y. Lan, Y. Xia, Q. Dai, P. He, Y. Zhang, Q. Zhao, J. Mao, Z. Lu, G. Liu, *Adv. Mater.* **2024**, *36*, 2310818.
[60] C.-C. Huang, W.-T. Chia, M.-F. Chung, K.-J. Lin, C.-W. Hsiao, C. Jin, W.-H. Lim, C.-C. Chen, H.-W. Sung, *J. Am. Chem. Soc.* **2016**, *138*, 5222.

[61] L.-H. Liu, Y.-H. Zhang, W.-X. Qiu, L. Zhang, F. Gao, B. Li, L. Xu, J.-X. Fan, Z.-H. Li, X.-Z. Zhang, *Small* **2017**, *13*, 1701621.
[62] S. Liu, H. Lai, F. Xing, P. Xiao, *Eur. Polym. J.* **2022**, *177*, 111458.
[63] C. Du, X. Guo, X. Qiu, W. Jiang, X. Wang, H. An, J. Wang, Y. Luo, Q. Du, R. Wang, C. Cheng, Y. Guo, H. Teng, H. Ran, Z. Wang, P. Li, Z. Zhou, J. Ren, *Adv. Sci.* **2024**, *11*, 2306031.
[64] S. Gao, Y. Jin, K. Ge, Z. Li, H. Liu, X. Dai, Y. Zhang, S. Chen, X. Liang, J. Zhang, *Adv. Sci.* **2019**, *6*, 1902137.
[65] R. Cui, J. Shi, Z. Liu, *Dalton Trans.* **2021**, *50*, 15870.
[66] L. Ruan, G. Song, X. Zhang, T. Liu, Y. Sun, J. Zhu, Z. Zeng, G. Jiang, *Biomater. Sci.* **2021**, *9*, 6830.
[67] X. Feng, T. Lin, D. Chen, Z. Li, Q. Yang, H. Tian, Y. Xiao, M. Lin, M. Liang, W. Guo, P. Zhao, Z. Guo, *Acta Biomater.* **2023**, *160*, 211.
[68] M. Wang, L. Zhang, H. Hao, X. Hu, Z. Xin, Y. Zhu, Y. Shen, J. Wang, *Colloids Surf., B.* **2022**, *213*, 112412.
[69] Q. Liu, Y. Xiang, Q. Yu, Q. Lv, Z. Xiang, *Sci. Rep.* **2024**, *14*, 3328.
[70] Y. Han, J. Ouyang, Y. Li, F. Wang, J. H. Jiang, *ACS Appl. Mater. Interfaces* **2020**, *12*, 288.
[71] a) J. Liu, Y. Jin, Z. Song, L. Xu, Y. Yang, X. Zhao, B. Wang, W. Liu, K. Zhang, Z. Zhang, J. Shi, *Chem. Eng. J.* **2021**, *411*, 128440; b) D. Guo, X. Dai, K. Liu, Y. Liu, J. Wu, K. Wang, S. Jiang, F. Sun, L. Wang, B. Guo, D. Yang, L. Huang, *Adv. Healthcare Mater.* **2023**, *12*, 2202424; c) J. An, M. Liu, L. Zhao, W. Lu, S. Wu, K. Zhang, J. Liu, Z. Zhang, J. Shi, *Adv. Funct. Mater. 32*, 2411568.
[72] a) M. C. Asensio-López, F. Soler, D. Pascual-Figal, F. Fernández-Belda, A. Lax, *PLoS One* **2017**, *12*, 0172803; b) M. Kciuk, A. Gielecińska, S. Mujwar, D. Kołat, Ż. Kałuzińska-Kołat, I. Celik, R. Kontek, *Cells* **2023**, *12*, 659.
[73] a) S. Qin, J. Xue, E. Jia, N. Ren, Y. Dong, C. Zhou, *Front. Oncol.* **2021**, *11*, 777295; b) Y. Zeng, Y. Zhan, X. Liu, J. Ma, H. Liu, H. Li, T. Yi, Q. Zhu, G. Du, L. Zhao, D. Chen, X. Chen, *Chem. Eng. J.* **2022**, *448*, 137724.
[74] a) S. Gao, X. Lu, P. Zhu, H. Lin, L. Yu, H. Yao, C. Wei, Y. Chen, J. Shi, *J. Mater. Chem. B.* **2019**, *7*, 3599; b) F. Zhang, C. Xin, Z. Dai, H. Hu, Q. An, F. Wang, Z. Hu, Y. Sun, L. Tian, X. Zheng, *ACS Appl. Mater. Interfaces* **2022**, *14*, 40633.
[75] C. Huang, B. Lin, C. Chen, H. Wang, X. Lin, J. Liu, Q. Ren, J. Tao, P. Zhao, Y. Xu, *Adv. Mater.* **2022**, *34*, 2207593.
[76] G. An, H. Zheng, L. Guo, J. Huang, C. Yang, Z. Bai, N. Wang, W. Yang, Y. Zhu, *J. Colloid Interface Sci.* **2024**, *662*, 298.
[77] A. D. Bokare, W. Choi, *J. Hazard. Mater.* **2014**, *275*, 121.
[78] Y. Ma, Z. Su, L. Zhou, L. He, Z. Hou, J. Zou, Y. Cai, D. Chang, J. Xie, C. Zhu, *Adv. Mater.* **2022**, *34*, 2107560.
[79] a) H. Wang, Z. Ma, *Biosens. Bioelectron.* **2020**, *169*, 112644; b) C. Chen, Y. Tan, T. Xu, Y. Sun, S. Zhao, Y. Ouyang, Y. Chen, L. He, X. Liu, H. Liu, *Langmuir* **2022**, *38*, 12307; c) M. Fu, P. Zhou, W. Sheng, Z. Bai, J. Wang, X. Zhu, L. Hua, B. Pan, F. Gao, *Anal. Chem.* **2024**, *96*, 4213; d) Y. Zu, Y. Wang, H. Yao, L. Yan, W. Yin, Z. Gu, *ACS Appl. Bio Mater.* **2022**, *5*, 1779; e) Y. Huang, L. Qi, Z. Liu, Y. Jiang, J. Wang, L. Liu, Y. Li, L. Zhang, G. Feng, *ACS Appl. Mater. Interfaces* **2023**, *15*, 35986; f) J. Huang, Y. Yao, Y. Chen, T. Lin, L. Hou, D. Tang, *Biosensors* **2022**, *12*, 830; g) D. Wei, D. Xiong, N. Zhu, Y. Wang, X. Hu, B. Zhao, J. Zhou, D. Yin, Z. Zhang, *Anal. Chem.* **2022**, *94*, 12981.
[80] M. Li, X. Lan, X. Han, S. Shi, H. Sun, Y. Kang, J. Dan, J. Sun, W. Zhang, J. Wang, *ACS Appl. Mater. Interfaces* **2021**, *13*, 29269.
[81] F. Liu, T. He, S. Gong, M. Shen, S. Ma, X. Huang, L. Li, L. Wang, Q. Wu, C. Gong, *Acta Biomater.* **2022**, *154*, 510.
[82] X. Tian, H. Xu, F. Zhou, X. Gong, S. Tan, Y. He, *Chem. Mater.* **2024**, *36*, 815.
[83] Y. Xiong, Z. Yong, S. Li, Q. Wang, X. Chen, Z. Zhang, Q. Zhao, Q. Deng, X. Yang, Z. Li, *Adv. Funct. Mater.* **2024**, *34*, 2310158.
[84] F.-T. Cheng, Y.-D. Geng, Y.-X. Liu, X. Nie, X.-G. Zhang, Z.-L. Chen, L.-Q. Tang, L.-H. Wang, Y.-Z. You, L. Zhang, *Nanoscale Adv.* **2023**, *5*, 3336.
[85] X. He, M. Li, S. Fan, Y. Li, L. Fang, G. Xiang, T. Yang, *Chem. Eng. J.* **2024**, *481*, 148522.
[86] Y. Hong, Q. Tao, Y.-Y. Liu, Z. Wang, H. Wang, L. Sun, *Dalton Trans.* **2022**, *51*, 11325.
[87] T. Li, M. Rong, Y. Wang, W. Sun, L. Lu, *J. Mater. Chem. B.* **2024**, *12*, 2537.
[88] S. Yu, H. Ni, X. Xu, Y. Cai, J. Feng, J. Zhang, *ACS Biomater. Sci. Eng.* **2023**, *9*, 6425.
[89] Z. Xin, Y. Shen, H. Hao, L. Zhang, X. Hu, J. Wang, *Colloids Surf., B* **2022**, *218*, 112776.
[90] L. Wang, X. Chen, C. Yan, *Genes Dis.* **2022**, *9*, 334.
[91] F. Auzel, *Chem. Rev.* **2004**, *104*, 139.
[92] V. Kannappan, M. Ali, B. Small, G. Rajendran, S. Elzhenni, H. Taj, W. Wang, Q. P. Dou, *Front. Mol. Biosci.* **2021**, *8*, 741316.
[93] N. Wu, Y. Tu, G. Fan, J. Ding, J. Luo, W. Wang, C. Zhang, C. Yuan, H. Zhang, P. Chen, *Asian J. Pharm. Sci.* **2022**, *17*, 253.
[94] Y. Sun, L. Qin, Y. Yang, J. Gao, Y. Zhang, H. Wang, Q. Wu, B. Xu, H. Liu, *Small* **2024**, *20*, 2402320.
[95] C. Bergs, P. Simon, Y. Prots, A. Pich, *RSC Adv.* **2016**, *6*, 84777.
[96] a) H. Bai, X. Liu, *Mater. Lett.* **2010**, *64*, 341; b) Q. Drmosh, M. Gondal, Z. Yamani, T. Saleh, *Appl. Surf. Sci.* **2010**, *256*, 4661; c) M. Sun, W. Hao, C. Wang, T. Wang, *Chem. Phys. Lett.* **2007**, *443*, 342.
[97] Y. Wolanov, P. V. Prikhodchenko, A. G. Medvedev, R. Pedahzur, O. Lev, *Environ. Sci. Technol.* **2013**, *47*, 8769.
[98] Z. Tang, S. Wu, P. Zhao, H. Wang, D. Ni, H. Li, X. Jiang, Y. Wu, Y. Meng, Z. Yao, *Adv. Sci.* **2022**, *9*, 2201232.
[99] D.-Y. Zhang, F. Huang, Y. Ma, G. Liang, Z. Peng, S. Guan, J. Zhai, *ACS Appl. Mater. Interfaces* **2021**, *13*, 17392.
[100] M. Xu, Y. Liu, W. Luo, F. Tan, D. Dong, W. Li, L. Wang, Q. Yu, *J. Colloid Interface Sci.* **2023**, *630*, 804.
[101] Y. Jiang, K. Shao, F. Zhang, T. Wang, L. Han, X. Kong, J. Shi, *Aggregate* **2023**, *4*, e321.
[102] J. Liu, Y. Yue, L. Ge, P. Chen, F. Tan, W. Wang, X. Wang, X. Qiao, *Colloids Surf., A.* **2020**, *607*, 125499.
[103] L. Gan, Y. Xia, J. Lv, J. Xie, Y. Yan, Y. Chen, *Colloids Surf., B.* **2024**, *241*, 114070.
[104] a) D. Wu, Y. Bai, W. Wang, H. Xia, F. Tan, S. Zhang, B. Su, X. Wang, X. Qiao, P. K. Wong, *J. Hazard. Mater.* **2019**, *374*, 319; b) X. Sun, G. Zhang, X. Ding, Y. Liu, K. Chen, P. Shi, S. Zhang, *Mater. Chem. Front.* **2022**, *6*, 956.
[105] C. Li, W. Zhang, Y. Nie, X. Du, C. Huang, L. Li, J. Long, X. Wang, W. Tong, L. Qin, Y. Lai, *Adv. Mater.* **2024**, *36*, 2308875.
[106] X. Haixia, Z. Peng, L. Jiezhao, G. Huiling, C. Xie, W. Yihan, J. Yanglei, J. Li, C. Wang, X. Wenning, Z. Lixin, C. Liu, *ACS Appl. Mater. Interfaces* **2024**, *16*, 9626.

**Hélder A. Santos** obtained his Doctor of Science in Technology (chemical engineering) in 2007 from the Helsinki University of Technology. He then became a full professor in pharmaceutical nanotechnology at the University of Helsinki. Currently, he is a full professor and the head of the Department of Biomaterials and Biomedical Technology at the University Medical Center Groningen, University of Groningen, as well as the head of the Translational Bionanomicro Theragenerative Medicine Lab. His scientific expertise lies in the development of novel nanoparticles/nanomedicines, tissue engineering, and regenerative medicine for controlled drug delivery and therapy for cancer, diabetes, and cardiovascular diseases.

**Shahbazi** received his Ph.D. in 2015 from the University of Helsinki, Finland. He is currently an assistant professor at the University Medical Center Groningen and the program leader for NanoBioMed at the Personalized Medicine Research Institute Groningen (PRECISION), the Netherlands. He is also an honorary adjunct fellow at the Faculty of Health, University of Technology Sydney, Australia. His research interest lies in nano-based photo-active regenerative hydrogels and scaffolds for wound healing, bone repair, and cancer immunotherapy to shape the future of multifunctional medicines. He is also developing biomimetic and cell-based delivery formulations for the treatment of different diseases.